CrossMark

THE ALFALFA Hα SURVEY. I. PROJECT DESCRIPTION AND THE LOCAL STAR FORMATION RATE DENSITY FROM THE FALL SAMPLE

Angela Van Sistine[1,2,8], John J. Salzer[2,8], Arthur Sugden[3], Riccardo Giovanelli[4], Martha P. Haynes[4],
Steven Janowiecki[2,5], Anne E. Jaskot[6], and Eric M. Wilcots[7]

[1] Department of Physics, University of Wisconsin-Milwaukee, Milwaukee, WI 53211, USA
[2] Department of Astronomy, Indiana University, Bloomington, IN 47405, USA
[3] Department of Endocrinology, Beth Israel Deaconess Medical Center, Harvard Medical School, Boston, MA 02115, USA
[4] Center for Astrophysics and Planetary Science, Cornell University, Ithaca, NY 14853, USA
[5] International Centre for Radio Astronomy Research, University of Western Australia, 35 Stirling Highway, Crawley, WA 6009, Australia
[6] Department of Astronomy, Smith College, Northampton, MA 01063, USA
[7] Department of Astronomy, University of Wisconsin-Madison, Madison, WI 53706, USA

ABSTRACT

The ALFALFA Hα survey utilizes a large sample of H I-selected galaxies from the ALFALFA survey to study star formation (SF) in the local universe. ALFALFA Hα contains 1555 galaxies with distances between ∼20 and ∼100 Mpc. We have obtained continuum-subtracted narrowband Hα images and broadband R images for each galaxy, creating one of the largest homogeneous sets of Hα images ever assembled. Our procedures were designed to minimize the uncertainties related to the calculation of the local SF rate density (SFRD). The galaxy sample we constructed is as close to volume-limited as possible, is a robust statistical sample, and spans a wide range of galaxy environments. In this paper, we discuss the properties of our Fall sample of 565 galaxies, our procedure for deriving individual galaxy SF rates, and our method for calculating the local SFRD. We present a preliminary value of $\log(\mathrm{SFRD}[M_\odot \, \mathrm{yr}^{-1} \, \mathrm{Mpc}^{-3}]) = -1.747 \pm 0.018$ (random) ± 0.05 (systematic) based on the 565 galaxies in our Fall sub-sample. Compared to the weighted average of SFRD values around $z \approx 2$, our local value indicates a drop in the global SFRD of a factor of 10.2 over that lookback time.

Key words: galaxies: star formation – surveys

1. INTRODUCTION

It is a fundamental, overarching goal of astronomy to understand how the universe evolved to its current state. Now that we are able to observe galaxies at high redshift ($z \sim 10$), we are able to build a more complete picture of how the universe has changed throughout cosmic history.

The observed rate at which galaxies have been forming stars throughout cosmic history is an important parameter for cosmological models and simulations to match. Therefore, measuring the rate at which the universe formed stars throughout time is crucial to our understanding of the formation of stars and galaxies. In general, measurements of the star formation rate density (SFRD) as a function of lookback time have painted a consistent picture. While there is a lack of consensus with SFRD measurements at high redshift (e.g., Bouwens et al. 2011; Coe et al. 2013; Ellis et al. 2013; Oesch et al. 2014), the decline in the SFRD of the universe from $z \sim 1$–2 until $z = 0$ has been confirmed by many previous studies (e.g., Lilly et al. 1996; Madau et al. 1996; Hogg et al. 1998; Wilson et al. 2002; Hanish et al. 2006; Hopkins & Beacom 2006; Gunawardhana et al. 2013). Local SFRD measurements are roughly an order of magnitude lower than the SFRD at the peak of star formation (SF).

There is a significant scatter in the SFRD between different studies at all redshifts and there is a need for more precisely measured values. Local measurements of the SFRD are of particular importance because they anchor our understanding of the evolution of the cosmic star formation rate (SFR) from early times to today. Locally, measurements of the SFRD exhibit a large range in values, spanning more than a factor of three (e.g., Hopkins & Beacom 2006; Gunawardhana et al. 2013). Many studies attribute this scatter to possible biases in the sample selection techniques and SFR measurement uncertainties. Therefore, improving on both of these is necessary in order to more precisely measure the local SFRD.

We have known for some time that most galaxy catalogs are deficient in some way (e.g., Disney & Phillipps 1983; Impey & Bothun 1997). Optical surveys are excellent at detecting bright spirals and luminous ellipticals, but often do not have sufficient sensitivity to detect low surface brightness (LSB), dwarf, and compact galaxies. Non-optical wavelength regimes provide a more panchromatic view of the extragalactic sky, but also have their own limitations and biases. For example, catalogs that select galaxies based on far-infrared (IR) and ultraviolet (UV) surveys may be biased based on dust content.

For estimates of the local SFRD, past studies have employed a variety of sample selection methods. Many studies have adopted values obtained using objective-prism samples of emission-line galaxies (e.g., Gallego et al. 1995, 2002; Gronwall 1999; Pérez-González et al. 2013). Other studies have selected samples using continuum emission at UV (e.g., Sullivan et al. 2000), IR (e.g., Tresse & Maddox 1998), or optical wavelengths (e.g., Brinchmann et al. 2004; Nakamura et al. 2004; Westra et al. 2010; Gunawardhana et al. 2013). Additionally, neutral hydrogen (H I) 21 cm line emission has been used to select galaxy samples (e.g., Meurer et al. 2006). The ALFALFA Hα survey utilizes a sample of galaxies selected via H I emission.

H I emission is a reliable way to select all galaxies capable of making stars. Surveys that select galaxies via their H I 21 cm emission have recently grown in importance (e.g., Barnes et al. 2001; Lang et al. 2003; Giovanelli et al. 2005). Problems that have long plagued other galaxy catalogs (lack of sensitivity to dwarfs, LSB galaxies, and compact galaxies; biases with respect to dust content) are less of a factor for H I-selected galaxy samples for many reasons. (1) Due to the ubiquitous presence of H I gas in galaxies later than S0, blind H I surveys are sufficiently sensitive to regularly detect even dwarf and LSB galaxies with small amounts of H I. (2) While not all types of galaxies are detected in H I (e.g., ellipticals), nearly all galaxies capable of making stars have neutral gas. (3) Blind H I surveys are unbiased by the optical and dust characteristics of the galaxy. Early-type galaxies aside, H I-selected samples are more inclusive than optical surveys of similar depth, and are more likely to include galaxies that have been historically under-represented in optical catalogs.

The current study is based on an H I-selected sample derived from the the Arecibo Legacy Fast ALFA (ALFALFA) survey catalog. The ALFALFA survey (Giovanelli et al. 2005; Haynes et al. 2011) is a wide-field H I survey. The ALFALFA sample improves upon the HI Parkes All-Sky Survey (HIPASS; Meyer et al. 2004) in two key aspects: (1) ALFALFA is much more sensitive than HIPASS (the ALFALFA catalog contains 29 times more objects per deg^2 than the HIPASS catalog), and (2) the relative beam sizes (15$'$.5 for Parkes, 3$'$.5 for Arecibo) mean that confusion effects (i.e., having more than one H I emitter in the beam at a given time) are greatly diminished in the nearby volume sampled by the ALFALFA Hα survey.

Determining the SF history of the universe is a multi-wavelength effort, as there are many different ways to measure SF. Each measurement method has its own intrinsic advantages and disadvantages and is often highly limited based on the target redshift being studied. All methods must make assumptions to convert from the directly measured quantity to a SFR. While some assumptions are unique to each SFR measure, all measures include an assumption about the shape of the initial mass function (Kennicutt & Evans 2012).

Continuum emission associated with SF is seen at wavelengths ranging from the radio to gamma-rays. Both UV and IR continuum radiation are commonly used SF measures (e.g., Meurer et al. 1999; Daddi et al. 2007; Salim et al. 2007). UV and IR measurements may also be used in conjunction (e.g., Buat et al. 2011) to measure both the emitted UV radiation and the absorbed UV radiation (re-emitted in the IR). Radio continuum emission also traces SF (e.g., Yun et al. 2001; Bell 2003). This continuum emission may be observed from the ground and is not significantly affected by dust. A tight correlation exists between radio emission and far-IR emission (e.g., Condon 1992), although both measures break down in certain regimes, for example, in low-IR-luminosity galaxies without significant dust (Bell 2003). X-ray based SFR measurements are based on the correlation of X-ray emission with far-IR and radio emission (e.g., Ranalli et al. 2003). If a galaxy does not contain an active galactic nucleus (AGN), X-ray emission traces the young stellar population. Gamma ray bursts that occur with core-collapse supernovae can also be used as an SF tracer (e.g., Kistler et al. 2009) once known biases are accounted for (e.g., Yüksel et al. 2008).

H II regions produce nebular emission lines across the spectrum. At optical wavelengths, hydrogen recombination lines such as Balmer series emission and forbidden emission lines such as [O II] and [O III] all indicate the presence of massive stars and therefore can be used to measure the SFR. While spectroscopic measurement of these lines can yield accurate SFRs, a spectroscopic slit or fiber will only capture the light from one or a few H II regions within a typical nearby spiral galaxy. To measure a *global* SFR for a spatially extended galaxy, it is necessary to use narrowband imaging to measure these emission lines (e.g., James et al. 2004; Meurer et al. 2006; Kennicutt et al. 2008).

This study uses Hα narrowband imaging to measure SFR. Hα is a reliable SF tracer (e.g., Moustakas et al. 2006). McQuinn et al. (2010) find that Hα accurately measures the SFR if changes to the SFR occur on timescales longer than 4–10 Myr. Hα emission is located in the red part of the optical spectrum, making it less affected by dust absorption than bluer emission lines (e.g., [O II], [O III], and Hβ emission). Compared to emission lines that originate from collisional excitation, Hα emission is relatively unaffected by ISM conditions such as metallicity and electron temperature (Osterbrock & Ferland 2006). Also, Hα is particularly useful for studies of the nearby universe, as it can be observed using ground-based optical telescopes.

Meurer et al. (2006) carried out an Hα imaging study for galaxies selected from HIPASS. Their project, known as the Survey for Ionization in Neutral-Gas Galaxies (SINGG), produced a preliminary estimate of the SFRD based on 111 HIPASS galaxies (Hanish et al. 2006). While the goals of the SINGG project are similar to ours, the properties of our galaxy sample are quite different. The SINGG sample consists primarily of galaxies with distances under ~25 Mpc; 70% of its galaxies have recession velocities less than 1800 km s^{-1}. The small sample size of this preliminary SINGG "SR1" sample, as well as its nearby nature, leads to larger uncertainties on their derived local SFRD.

In addition to measuring the local SFRD, the ALFALFA Hα survey data will also be useful for a number of additional important science applications, including studying the modes of SF in a relatively unbiased sample of galaxies, obtaining targets for follow-up spectroscopic observations to derive metal abundances, the detection of isolated point sources of line emission, studying the impact of environment on SF, and comparing SFRs at different wavelengths. In addition to this study, other studies have utilized the ALFALFA data set to study properties of the galaxy population seen by ALFALFA (Huang et al. 2012), SF in cluster galaxies (Gavazzi et al. 2012, 2013), and the galaxies included in the overlap region of ALFALFA, SDSS, and *GALEX* (GASS; Catinella et al. 2010; Schiminovich et al. 2010).

The ALFALFA survey, our sample selection, and the H I properties of our sample are described in Section 2. We describe our data, observing strategies, and our derivation of Hα luminosities in Section 3. In Section 4, we outline the completeness and large-scale structure (LSS) corrections necessary to deriving the local SFRD. In Section 5 we derive a preliminary local SFRD based on our Fall sample and describe and quantify our errors. In Section 6, we discuss our measurement of the local SFRD and some of the many additional applications of our sample. We summarize this work in Section 7. Throughout this paper we assume $H_0 = 70$ km s^{-1} Mpc^{-1}, $\Omega_0 = 0.3$, and $\Omega_\Lambda = 0.7$.

2. SAMPLE SELECTION

2.1. The ALFALFA Survey

The ALFALFA survey is a blind 21 cm H I survey that was carried out at the Arecibo 305 m radio observatory in Puerto Rico. It covers a large area of the sky at high Galactic latitude ($\sim$7000 deg^2), detects H I masses down to $10^6 M_\odot$, has a velocity resolution of 11 km s^{-1}, and an angular resolution of $\sim$4′. For the complete details of the ALFALFA survey method, sensitivity limits, and potential uses of the data see the survey description paper (Giovanelli et al. 2005).

In 2011, the ALFALFA survey team released a data set comprising 40% of the total survey area: the α.40 catalog. Complete details on the catalog are given in the α.40 paper (Haynes et al. 2011). Here, we briefly summarize one aspect of the ALFALFA survey that is important to our Fall sample selection process. ALFALFA assigns a code to each galaxy indicating the confidence level of the detection. Code 1 objects have signal-to-noise ratio (S/N) values above 6.5; code 2 objects have $4.5 <$ S/N < 6.5 but possess a prior confirming redshift (for details see Saintonge 2007 and Haynes et al. 2011). For our sample, we chose to include both code 1 and 2 objects. It is appropriate to note that the code 2 objects *could* represent a biased sample because they require prior redshift detection. Out of the 565 galaxies in our Fall volume, only 17 are code 2 objects. Nevertheless we compute our final SFR densities in two ways: using our entire Fall sample (both code 1 and 2 objects) and using *only* code 1 objects in case the code 2 objects bias our sample in any way.

The ALFALFA Hα sample was selected from the α.40 data release. We describe our Fall sample selection, including our treatment of code 1 and 2 objects, in the following subsection.

2.2. The ALFALFA Hα Sample Selection Criteria

Our sample selection was strongly influenced by our goal of minimizing traditional biases and uncertainties associated with measuring the local SFRD. To achieve this we designed our sample to be *as close to volume-limited* as possible to minimize any incompleteness corrections. Additionally, to limit any bias due to LSS variations, we also excluded the Local Supercluster and the Virgo cluster, both known density enhancements, from our sample. We also chose a sample size and volume that would be manageable but large enough to provide good statistics. Our resulting sample is largely representative of the galaxy distribution found in the local universe.

Our entire sample is selected from the ALFALFA α.40 catalog by constraining the R.A., decl., velocity, and code designation. We sub-divide our sample into two volumes based on R.A.: the Spring sample and Fall sample. Figures 1 and 2 show the position-redshift diagrams for α.40 galaxies in our sample regions. For both our Spring and Fall samples, we selected both code 1 and 2 objects and set a minimum recession velocity of 1460 km s^{-1} ($\sim$20 Mpc; the green dashed lines in Figures 1 and 2). For our primary narrowband Hα filter set, this velocity represents the inner velocity limit of the first non-rest-frame Hα narrowband filter (see Section 3.1). We did not use the rest frame Hα filter because we designed our sample to exclude the Local Supercluster. In addition, we wanted to avoid contamination caused by stellar emission lines (e.g., from dMe stars). Another motivation for excluding lower-velocity objects is the greater effect of peculiar velocities on galaxies with low recession velocities, which results in less-precisely known
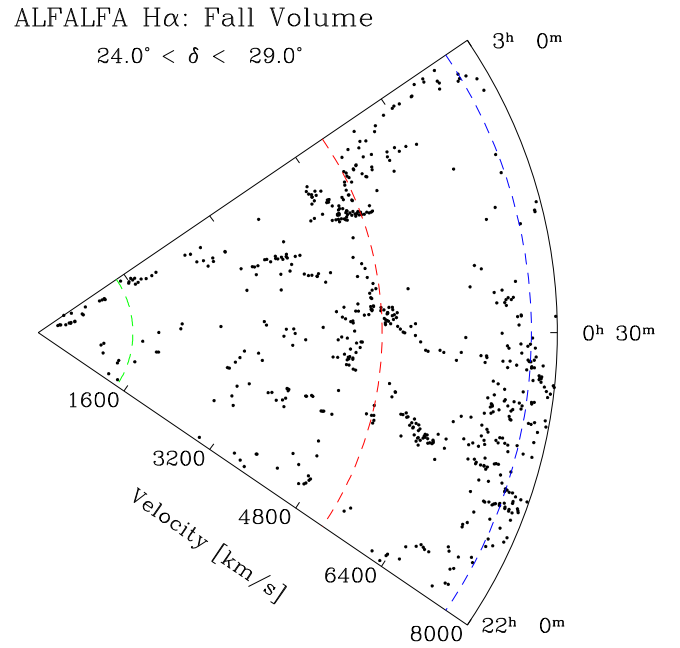

Figure 1. A position-redshift diagram showing the α.40 sample in the area of the sky that includes our Fall sample. The dashed green line is our inner velocity limit, the dashed blue line is our outer velocity limit, and the dashed red line is our previous outer velocity limit at 5300 km s^{-1}.
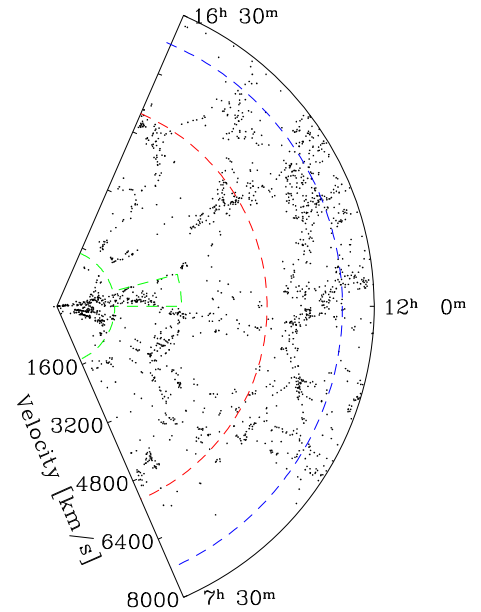

Figure 2. A position-redshift diagram showing the α.40 sample in the area of the sky that includes our Spring sample. The dashed lines are the same as in Figure 1. The Spring volume excludes the Virgo cluster region that is represented by the extension of the green (inner velocity limit) line between right ascensions of 12^h and 13^h.

distances. We also exclude the Virgo galaxy cluster from our sample. The Virgo cluster has a mean recession velocity of $\sim$1080 km s^{-1} and a velocity dispersion of $\sim$630 km s^{-1} (Fadda et al. 1996). Therefore, we extended our minimum velocity to 3140 km s^{-1} (the edge of one of our Hα filters) for

Table 1
ALFALFA Hα Filters

Filter Name	λ_c	$\Delta\lambda$	λ_{min}	λ_{max}	v_{min}	v_{max}	k
KP1563	6573	67	6548	6595	−680	1460	0.095
KP1564	6618	74	6595	6632	1460	3140	0.092
KP1565	6659	68	6632	6679	3140	5300	0.090
KP1566	6707	71	6679	6734	5300	7810	0.087
Y006	6577	59	6558	6599	−220	1650	0.094
Y007	6618	60	6599	6638	1650	3430	0.092
Y008	6658	60	6638	6679	3430	5300	0.090
Y009	6700	63	6679	6722	5300	7260	0.088
Y010	6742	60	6722	6766	7260	9270	0.085

Note. The narrowband Hα filters used for the ALFALFA Hα Survey. Wavelengths and full-width half-maxima ($\Delta\lambda$) are in Angstroms and velocities are in units of km s^{-1}. λ_c is the central wavelength of the filter and λ_{min} and λ_{max} are the minimum and maximum wavelengths of the Hα line observable in each filter, respectively. The corresponding minimum and maximum recession velocities observable with each filter are shown as v_{min} and v_{max}, respectively. The extinction coefficients, k, used for each filter, are listed in the last column.
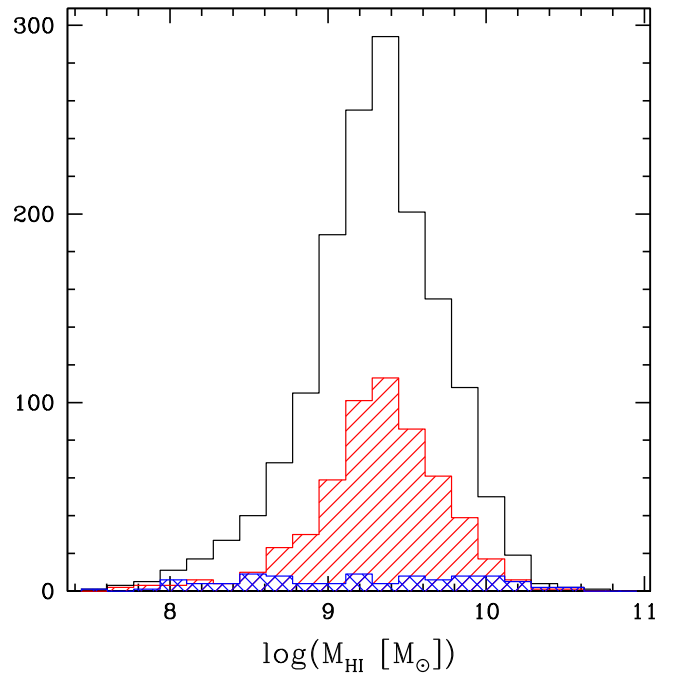

Figure 3. A histogram of the H I masses included in our galaxy sample. Black indicates our total sample, red shows our Fall sample distribution, and blue shows the SINGG sample from Hanish et al. (2006).

right ascensions between 12^h and 13^h. Our exclusion of the Virgo cluster region is shown in Figure 2 as an extension of our minimum velocity (green line) between 12^h and 13^h.

We chose the outer velocity limits of our sample to create a manageable sample size as well as a large enough volume to reduce any bias due to large scale density variations. The outer velocity limit is 7600 km s^{-1} for our Fall sample and 7200 km s^{-1} for our Spring sample (∼100 Mpc; the blue dashed lines in Figures 1 and 2). These outer velocity limits are larger than the outer velocity limit of our original survey design, 5300 km s^{-1}, for both the Fall and Spring samples (∼75 Mpc; the red dashed lines in Figures 1 and 2). Our original sample, which we call the Phase I sample, had a 5300 km s^{-1} limit for practical purposes in that it was the velocity cutoff for Hα detection between narrowband filters (see Table 1). However, after examining our sample it became clear that this limit was not sufficient to cover a truly representative range of environmental densities due to the LSS in the local universe. Therefore, we expanded both our Fall and Spring samples to achieve a fairer sampling of the local galaxy distribution as well as to increase our sample size. We call this expanded sample "Phase II." The Phase II survey expansion has proven effective at achieving these goals. As we will show in Section 5, the average volume density of our Fall sample is very close to the global volume density. That is, the ratio of the volume density of the entire α.40 catalog out to 9500 km s^{-1} to the volume density of the Fall sample is close to unity. Figures 1 and 2 illustrate how our velocity limit choices allow for coverage of both highs and lows of galaxy environmental density. The velocities shown in Figures 1 and 2 are heliocentric, however, we note that we use cosmic microwave background (CMB) rest-frame velocities when calculating our sample volumes.

Our Fall sample includes all ALFALFA galaxies in our velocity range with right ascensions between 22^h and 03^h 04^m, the full R.A. range of ALFALFA in the Fall sky, and declinations between +24° and +29°. The Fall sky sample has an area of 339.97 deg^2, a volume of 39,435 Mpc^3, and contains 565 ALFALFA sources with code designations of 1 or 2.

2.3. The ALFALFA Hα Sample H I Properties

Our entire sample includes a total of 1555 galaxies, 565 in the Fall sample and 990 in the Spring sample. In this section we present the relevant ALFALFA-derived properties of the ALFALFA Hα survey and our Fall sub-sample. Additionally, to demonstrate how our sample is improving upon past studies, we compare our survey to another recent H I-selected, Hα galaxy survey: SINGG (Meurer et al. 2006). The SINGG sample includes galaxies with H I masses above $10^7\,M_\odot$ and distances out to 73 Mpc, with the majority of galaxy distances less than ∼25 Mpc. There are a total of 468 galaxies in the SINGG sample which were selected from HIPASS (Meyer et al. 2004), 111 of which have published Hα observations (Hanish et al. 2006) and are used for comparison here.

Figure 3 shows that the H I masses of the full ALFALFA Hα sample in black and the Fall sample in red. Our entire sample spans over three orders of magnitude. Additionally, the sample appears to be complete to ∼$10^{9.3}\,M_\odot$. That is, we are not missing any galaxies in our volume with H I masses above ∼$10^{9.3}\,M_\odot$. The majority of galaxies in the ALFALFA Hα sample have H I masses below the the knee of the HI mass function (HIMF) ($10^{9.96}\,M_\odot$; Martin et al. 2010) and therefore the sample includes a significant portion of the galaxies in this populous region of the HIMF. Figure 3 also shows how the H I mass distribution of galaxies in the ALFALFA Hα survey differs from that of the SINGG galaxies (in blue). Though our sample covers the same H I mass range as the SINGG sample, the SINGG sample includes a higher proportion of low-mass galaxies ($M_{H\,I} < 10^{8.5}\,M_\odot$) than our sample. This is because the SINGG sample includes galaxies with distances less than our minimum distance, ∼20 Mpc (see Figure 4). In addition, the SINGG sample was constructed in such a way as to have roughly equal numbers of galaxies per decade of $M_{H\,I}$ (Meurer et al. 2006). While low-mass galaxies are far more populous than higher-mass galaxies, high-mass star-forming galaxies
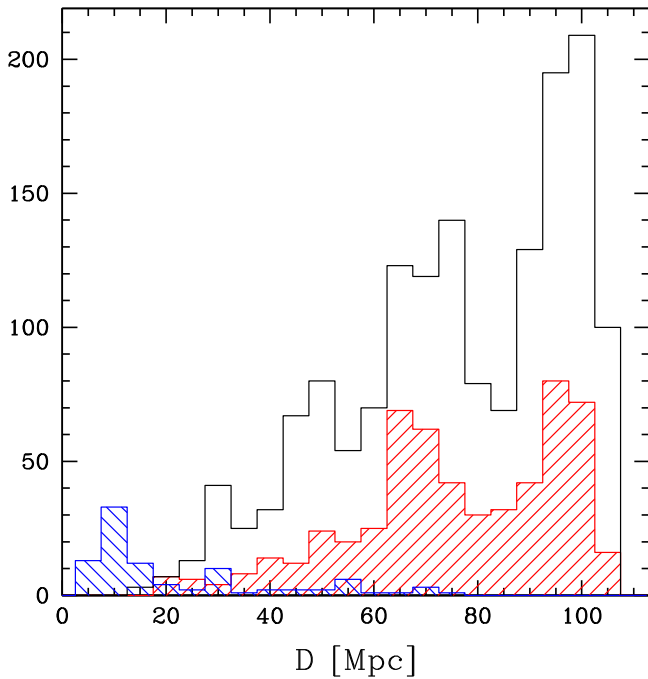
Figure 4. A histogram of the distances to galaxies included in our galaxy sample. Black indicates our total sample, red shows our Fall sample distribution, and blue shows the SINGG sample from Hanish et al. (2006).
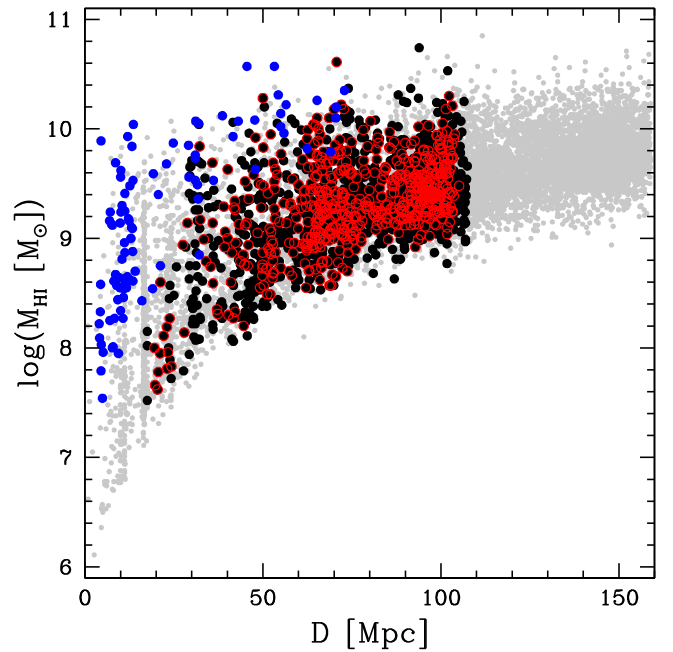

Figure 5. The H I mass as a function of distance for our sample. As in Figure 3, black indicates our total sample, red indicates our Fall sample, and the SINGG sample from Hanish et al. (2006) is in blue. The gray points are the entire α.40 sample. At all distances, our sample probes well below the knee of the H I mass function ($10^{9.96}\,M_\odot$).

contribute the majority of the SF (e.g., Brinchmann et al. 2004). Because the contribution of the low-mass galaxies to the local SFRD is small, the correction we must apply to compensate for the low-mass galaxies that fall below ALFALFA's detection limits at our sample distances is likewise small (see Section 4.1).

Figure 4 shows that the ALFALFA Hα sample and the Fall sample extend beyond the distance range of the SINGG sample. The majority of SINGG galaxies have distances closer than the minimum distance limit of our survey. Looking at our Fall sample, it is easy to see the presence of over- and underdensities due to LSS at different distances. It turns out that our Fall volume is close to a representative sample of the overall galaxy density in the nearby universe (for more detail see Sections 4.2 and 5).

Figure 5 shows a Spaenhauer diagram (Spaenhauer 1978; H I mass versus distance) of the ALFALFA Hα sample, the Fall sample, the Hanish et al. (2006) SINGG sample, and the entire α.40 sample, for comparison. As alluded to previously, the HIMF derived from the α.40 catalog has a characteristic H I mass of $\log(M_{\mathrm{H\,I}}^*[M_\odot]) = 9.96$ (Haynes et al. 2011). Our sample is complete to well below $M_{\mathrm{H\,I}}^*$ at all distances. The greater sensitivity and smaller beam size of the ALFALFA survey compared to the HIPASS survey allow our sample to include more galaxies out to greater distances than the SINGG sample while still sampling well below the knee of the HIMF. Our sample does not include the lowest H I mass galaxies found in ALFALFA due to our inner velocity limit. Our minimum H I mass is $M_{\mathrm{H\,I}} \sim 10^{7.5}\,M_\odot$ for both our Fall and Spring samples. Though our inner velocity limit excludes galaxies with the lowest H I masses, the volume excluded due to our inner velocity limit is small ($1216\,\mathrm{Mpc}^3$) compared to our total volume ($126,905\,\mathrm{Mpc}^3$). We discuss the effect that excluding this volume has on our local SFRD measurement in Section 5.

3. THE ALFALFA Hα SURVEY DATA

3.1. Observations and Image Processing

Optical observations for our project began in 2006 March with a pilot study and concluded in 2014 May. Our observing campaign primarily utilized the WIYN 0.9 m[9] located at Kitt Peak National Observatory (KPNO) to acquire our data. Starting in 2010, we also used the NOAO[10] 2.1 m at KPNO to observe many of our more distant Phase II objects. A large portion of our observations using the 2.1 m telescope were taken using time awarded to us through the NOAO Surveys program.

During our observing campaign, we used two different detectors at the 0.9 m telescope and three at the 2.1 m telescope. The majority of our survey images were taken using the S2KB detector on the 0.9 m telescope. S2KB had a field of view of 20′ on a side and a pixel scale of $0\rlap{.}''6\,\mathrm{pixel}^{-1}$. The Half-Degree Imager (HDI) was in use at the 0.9 m telescope only during our final observing season (spring 2014) and has a 29′ square field of view with a pixel scale of $0\rlap{.}''43\,\mathrm{pixel}^{-1}$. The detectors that we used on the 2.1 m had smaller fields of view, but finer pixel scales. T2KB was 10′ on a side, STA2 and STA3 both had fields of view of 10′ by $6\rlap{.}'6$. All of the detectors on the 2.1 m had pixel scales of $0\rlap{.}''3\,\mathrm{pixel}^{-1}$.
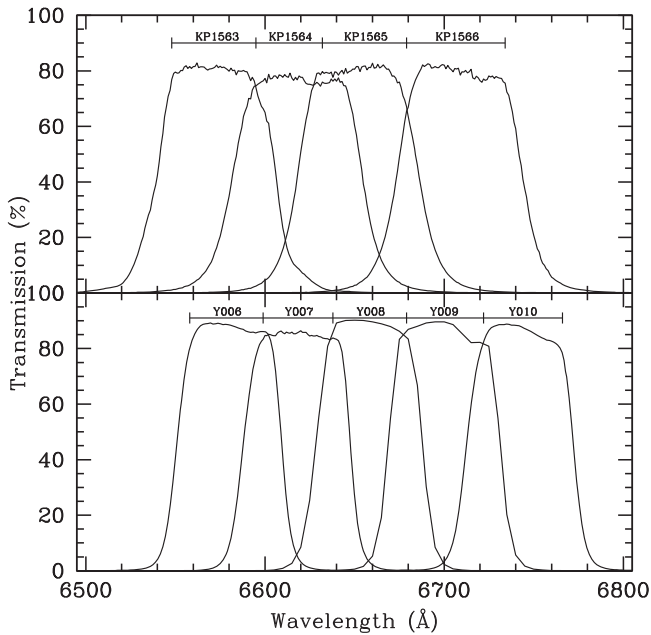
Figure 6. The filter transmissions for the Kitt Peak filter set (KP1563, KP1564, KP1565, KP1566) and the WIYN 0.9 m filter set (Y006, Y007, Y008, Y009, Y010). We show the wavelength divisions we use to determine our minimum and maximum velocities for each filter (values shown in Table 1).

We used two narrowband filter sets throughout our observing campaign (Table 1). Figure 6 shows the filter transmissions for our two different filter sets. The Kitt Peak filter set (filters beginning with "KP") was used on the 0.9 m telescope until the set was replaced by the WIYN filter set (filters beginning with "Y") in 2008. All of our 2.1 m telescope observations used the Kitt Peak filter set. Figure 6 also shows the wavelength ranges we used to determine which filter to observe each galaxy through. The wavelength cutoffs and their corresponding recessional velocities are shown in Table 1. Note that the third filter in each set has the same recessional velocity cutoff (5300 km s^{-1}); this was the limit of our original sample, what we call Phase I. Galaxies which have recession velocities greater than this cutoff are in our Phase II sample.

When deciding with which telescope to observe a particular target, we considered two factors. (1) The presence of targets located close to each other on the sky: the 0.9 m telescope has a larger field of view than the 2.1 m telescope. Therefore, we used the 0.9 m telescope to observe pairs of galaxies with similar velocities that could be observed in the same field of view (i.e., were separated by an angular distance less than the 0.9 m field of view). This helped reduce the overall telescope time necessary to observe our sample. (2) The recession velocity of the target: the 2.1 m was better suited to observe the more distant targets (Phase II) because of its larger diameter and finer pixel scale.

For each target galaxy, we obtained three images: two narrowband Hα images and one broadband R image. We used a standard sequence of Hα-R-Hα for our observations so that our R band image is bracketed (in time) by two Hα images. Our *total* exposure times were 40 minutes in Hα and 4 minutes in R for the 0.9 m telescope and 30 minutes in Hα and 3 minutes in R for the 2.1 m telescope.

We developed our own image reduction and analysis pipeline to create continuum-subtracted images as well as to standardize our photometry procedure. Both of these codes were developed

using IRAF[11] and will be described in detail in our forthcoming paper (A. Van Sistine et al. 2016, in preparation; hereafter Paper 2). We summarize this procedure below.

Prior to submitting images to our image analysis pipeline, we performed standard image reductions using IRAF. Mean bias image subtraction, overscan subtraction, flat field correction, and bad pixel cleaning were all performed in the standard manner. We used the L.A. Cosmic script (van Dokkum 2001) to remove cosmic rays from our images. Our analysis pipeline was designed to create measurement-ready, continuum-subtracted images. It takes as input the three reduced images for each galaxy and produces output images and data files. In particular, it produces a combined, continuum-subtracted Hα image and an R-band image as well as values necessary for subsequent flux calibration, such as the scale factor used during the continuum subtraction.

The first step carried out by our pipeline is to align the three images. Then, an astrometric solution is found using stars within the image and a world coordinate system (WCS) is created for the images. Next the code prepares the images for continuum subtraction. Using several stars near the target galaxy, the code measures the image resolution (the stellar point-spread function). If necessary, the code smooths images so that the FWHM of their point-spread functions match that of the image with the largest FWHM. The code then measures the fluxes of several stars near the galaxy and a mean scale factor for each image is computed. The first Hα image is given a scale factor of unity and the other images are scaled to the first such that the average flux levels of the measured stars are the same in all three images. The code then subtracts the scaled R-band image from each Hα image and combines the two continuum-subtracted images into a final Hα image. This final image, along with the *un-scaled R*-band image, are the images that are measured using our photometry code (described below). Our pipeline is interactive at all stages, allowing the user to select stars for alignment and scale-factor determination. It also allows the user to exclude outliers in the FWHM and scale factor calculation stages.

Examples of our continuum-subtracted Hα images and R-band images are shown in Figure 7. The top row of R-band images in Figure 7 shows a range of galaxy morphologies and luminosities. The lower row of images shows the large range of Hα line strengths we observe in our continuum-subtracted images. The vast majority (93%) of our images show some level of Hα emission. Only 6% of the ALFALFA sources in our volume show emission in R without emission in Hα. Images that show no R or Hα emission associated with the ALFALFA source are rare (~1%). H I sources without detectable R or Hα emission are potentially very interesting, however it is beyond the scope of this paper to explore these sources in detail. Possible candidates for these non-detections are ultra-compact high-velocity clouds (UCHVCs) and "almost dark" objects (see Adams et al. 2013, 2015; Giovanelli et al. 2013; Cannon et al. 2015, and Janowiecki et al. 2015 for examples of these types of sources).

Our photometry code will be described in detail in Paper 2; here we present a short summary of the relevant information. Our code allows us to interactively use circular apertures to measure the total narrowband and broadband flux of our target galaxies. The user selects a position around which a series of

---

[11] IRAF is distributed by the National Optical Astronomy Observatory, which is operated by the Association of Universities for Research in Astronomy (AURA) under cooperative agreement with the National Science Foundation.
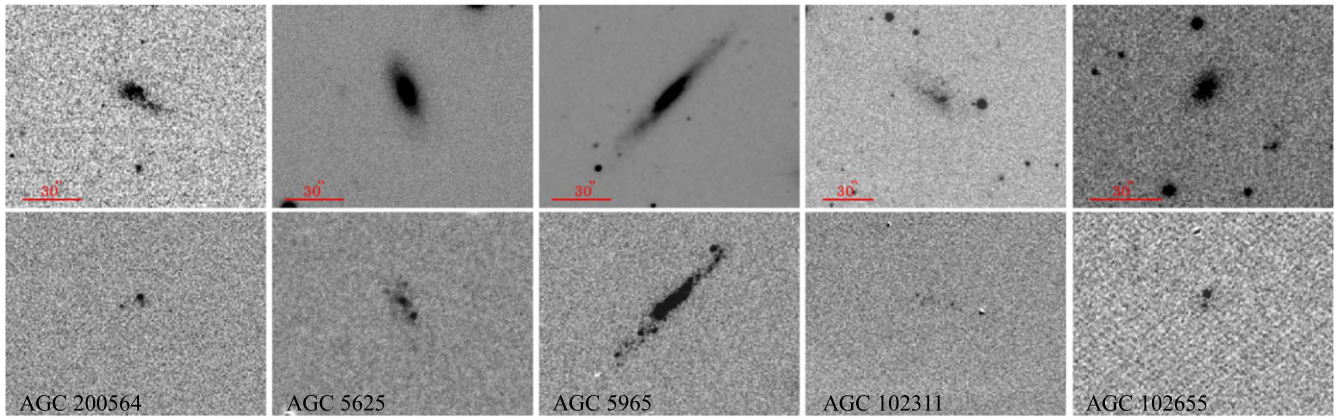
Figure 7. Examples of broadband R images and continuum-subtracted Hα images. Each column is an individual galaxy, the top row is the R-band image, and the bottom row is the final continuum-subtracted Hα image. The R-band images include a 30″ scale bar for reference.

circular apertures are displayed. The central location and diameter of the apertures can be changed as needed before the user selects the appropriate aperture. The code also allows the user to interactively mask any foreground stars or non-target galaxies that are within the aperture before performing photometry. We used only circular apertures as opposed to elliptical apertures to standardize and simplify our measurement procedure. We tested multiple aperture types: elliptical apertures, circular apertures, and multiple smaller apertures for larger galaxies with many distinct H II regions. These tests showed that there was no loss of precision and no significant decrease in the signal-to-noise of our fluxes using simple circular apertures as opposed to other types.

3.2. Off-Target Hα Emission Regions (OTHERs)

Because our primary science goal is to measure the local SFRD, it is important to measure *all* the SF in our volume, not just the SF from the ALFALFA targets. The effective ALFALFA beam is large ($\sim 4'$), therefore multiple galaxies can fall within a single detection if their velocities are similar. In addition, we occasionally observe Hα emission associated with a galaxy located far from the H I target (i.e., clearly in a separate, distinct galaxy). While not detected as separate sources in the ALFALFA survey, such sources are still star-forming galaxies within our survey volume. We call these "extra" emission sources OTHERs. We measure the fluxes of any OTHERs that are present in our continuum-subtracted images if their optical coordinates are within our survey area. In the Fall sample, 101 OTHERs have been detected ($\sim 15\%$ of Fall galaxies have OTHERs) and the combined Hα luminosity of all the OTHERs is $\sim 3\%$ of the combined Hα luminosity of all of the Fall target galaxies. An example of an OTHER is shown in Figure 8.

We do not know the redshifts or distances for the majority the OTHERs, but if the emission is Hα, we do know that their velocities must be within our volume because we observe Hα emission through a narrowband filter ($\Delta\lambda \sim 60$ Å). We use the Sloan Digital Sky Survey (SDSS; York et al. 2000) ninth data release (DR9; Ahn et al. 2012) and the NASA/IPAC Extragalactic Database[12] to determine if each OTHER has a

known redshift and to eliminate any higher-redshift sources with emission lines shifted into our narrowband filter (e.g., [O III]). If either SDSS or NED has a redshift determination, we adopt that recession velocity for the OTHER and adopt a distance assuming the Hubble flow. In cases where neither SDSS nor NED has a redshift determination, the OTHER is given the distance of the ALFALFA target with which it is associated.

If we do know the recession velocity of the OTHER, the ALFALFA target with which it is associated is simply the ALFALFA target with the closest physical distance. If we do not know the recession velocity, the OTHER is associated with the ALFALFA target with the closest angular distance to the OTHER and a recession velocity within the velocity limits of the narrowband filter within which the OTHER was detected. Many OTHERs appear to be either interacting with the ALFALFA target or part of a group with the ALFALFA target. Figure 9 shows the angular and projected physical separation between each OTHER in the Fall sample and its nearest ALFALFA target. The bulk (86%) of the OTHERs are within $5'$ of the nearest ALFALFA source. This in turn implies that the cataloged ALFALFA H I detection for these sources likely represents a composite detection of two (or more) galaxies located within the same beam (see Figure 8). In terms of projected distance, all but one of the OTHERs in our Fall sample are within ~ 170 kpc from the ALFALFA target with which they are associated. Additionally, the velocity differences between the OTHERs in our Fall volume and the nearest ALFALFA galaxy are less than 300 km s^{-1} for the three OTHERs with independent redshift information. This allows us to assume that even though the OTHERs are clearly distinct galaxies, they lie within the same ALFALFA H I detection and consequently are subject to the same selection function we use on our primary targets.

We do also observe point-like emission sources within our images in addition to the extended OTHERs. We term these objects "Hα dots" and we do not include them in the ALFALFA Hα Survey. They are not included because, without spectroscopic follow-up, there is no way to know if they are within our volume. A separate ongoing project (see Section 6) is utilizing follow-up spectra to characterize these objects. So far, 157 Hα dots have been observed spectroscopically. Of these, about half have redshifts that place them within our volume (i.e., the emission is Hα). Additionally, because these objects are point-like, excluding them has a negligible effect on

---

[12] The NASA/IPAC Extragalactic Database (NED) is operated by the Jet Propulsion Laboratory, California Institute of Technology, under contract with the National Aeronautics and Space Administration.
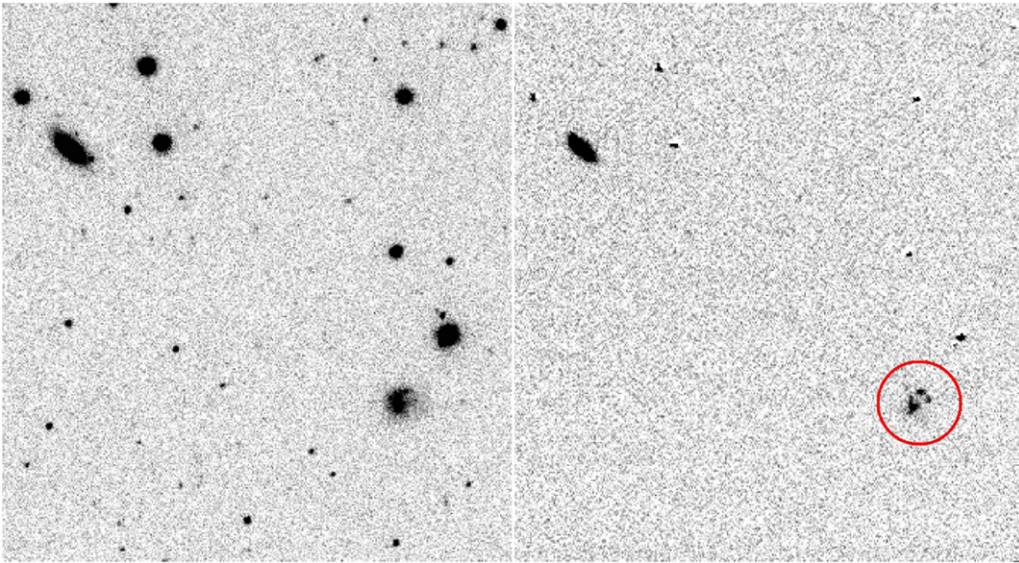
Figure 8. An example of an OTHER. Left: broadband *R* image. Right: continuum-subtracted narrowband Hα image. The OTHER is circled in red in the Hα image. The target galaxy, AGC 123178, is in the top left of the images. These two galaxies have an angular separation of $2\rlap{.}'3$ (i.e., less than the diameter of the ALFALFA beam) and a projected separation of 62 kpc.
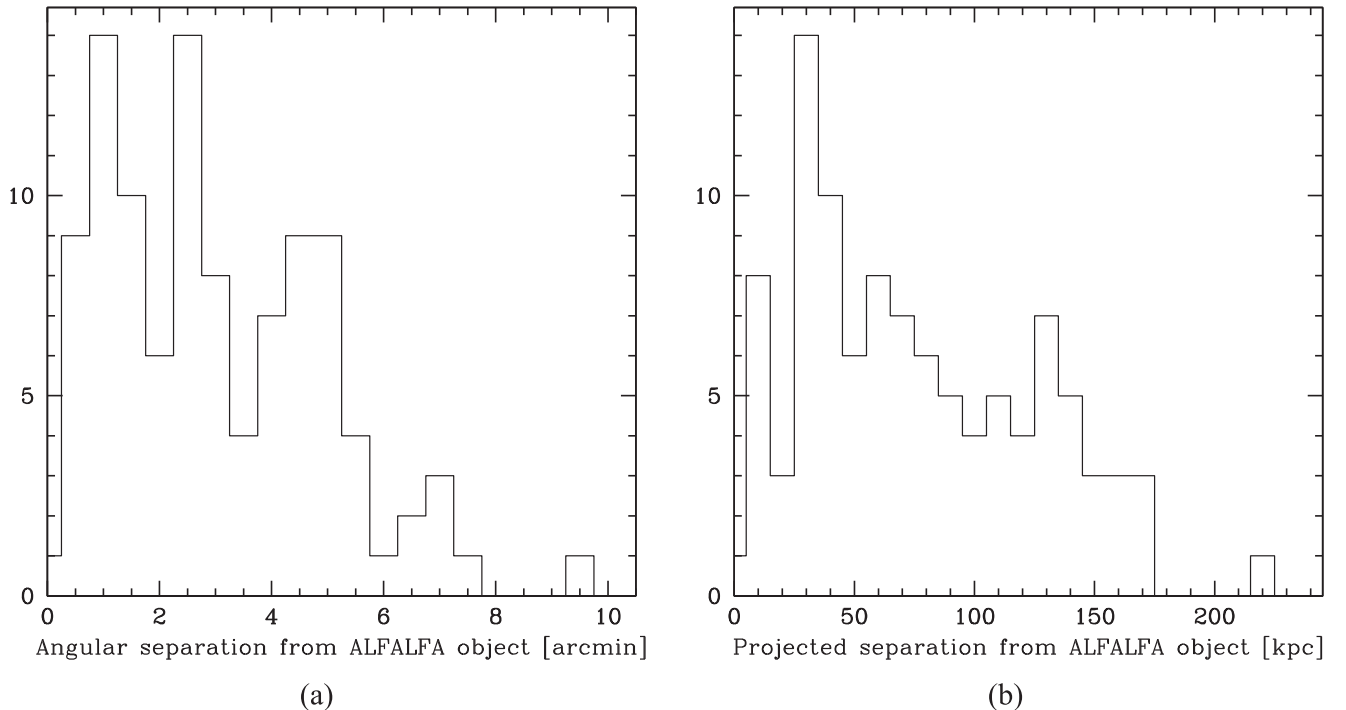

Figure 9. Histogram of the angular (a) and projected (b) separation of each OTHER from its associated ALFALFA galaxy. The projected separation assumes that the OTHERs are at the same distance as their associated ALFALFA galaxies. The vast majority of the extra emission sources are within 150 kpc and 5′ of their host ALFALFA galaxy. In addition, all OTHERs with known redshifts have velocities that are within 300 km s^{-1} from their associated galaxy. These facts allow us to assume that the vast majority of the OTHERs are part of the same H I detection as the ALFALFA galaxy in most cases.

our measurement of the total SF in our volume. For example, the combined flux from the 38 Hα dots with spectra that lie within the Fall survey volume is ~0.6% of the total Hα flux from the Fall target galaxies.

3.3. Flux Calibration and Corrections

In this section we describe our method for converting narrowband instrumental magnitudes to calibrated emission-

line fluxes. We take into account the differences in our broad- and narrowband filter bandpass and account for emission-line contamination from the Hα and [N II] emission lines that lie within our broadband *R* filter. Contamination of our fluxes due to emission from AGNs is minimal in our sample galaxies. We discuss how we handle AGN contamination effects in Section 4 and discuss the effects on the Fall sample in Section 5 and on the Spring sample in A. Van Sistine et al. (2016, in preparation; hereafter Paper 3).

We also correct our fluxes for Galactic absorption and make two statistical corrections: one to remove the [N II]$\lambda\lambda$6548, 6583 doublet flux from our continuum-subtracted Hα flux and another to correct for the dust absorption within the target galaxy. Our methods for the latter two corrections are very similar to the ones described in Kennicutt et al. (2008).

3.3.1. Narrowband Flux Determination

We relate our measured instrumental magnitude (m_i) to our calibrated magnitude (m_o) through the usual equation

$$m_o = m_i - Xk + ZP, \qquad (1)$$

where X is the airmass, k is the atmospheric extinction coefficient, and ZP is the nightly zero point derived from our spectrophotometric standard star observations. We do not use a color term in Equation (1) because we generally do not know the color of the galaxy from our data, but in any case the R-band color coefficient in our filter system is very small (well under 0.1), meaning that the color term will also be small.

To derive our atmospheric extinction coefficients, we interpolated the widely used extinction curve for KPNO for 3400–9000 Å at the central wavelengths of each of our filters (see Table 1).

If the original observation of a given galaxy was taken under non-photometric conditions, we also apply an additional correction to account for the presence of clouds. To determine this correction value, we take a short exposure (180 s) of the galaxy through the Hα filter during photometric conditions and use foreground stars common to both the original observation and the shorter calibration exposure to post-calibrate the flux of the galaxy. We select several stars in both frames and determine the average magnitude offset, PC, where PC $= m_{o,\mathrm{phot}} - m_{o,\mathrm{non\text{-}phot}}$. Therefore,

$$m_i = m_{i,\mathrm{non\text{-}phot}} + \mathrm{PC}. \qquad (2)$$

For further detail on our post-calibration procedure see Paper 2.

To convert from magnitudes to flux units, we use the monochromatic magnitude equation from Massey et al. (1988):

$$m_\nu = -2.5 \log(f_\nu) - 48.59, \qquad (3)$$

which can be expressed in terms of flux and transformed from frequency units to wavelength units using $\lambda_{\mathrm{H}\alpha} = 6562.82$ Å and $f_\lambda = c/\lambda^2 f_\nu$ as

$$f_\lambda = (\lambda_{\mathrm{H}\alpha}/\lambda)^2 10^{-0.4 m_\nu - 8.593 + \log(\Delta\lambda)} [\mathrm{erg\ s}^{-1}\,\mathrm{cm}^{-2}], \qquad (4)$$

where $\Delta\lambda$ is the narrowband filter width in Å (see Table 1).

We next apply a correction for filter transmission following the methodology in Kennicutt et al. (2008):

$$f_{\mathrm{H}\alpha+[\mathrm{N\,II}]} = f_\lambda \cdot \left[T_{\mathrm{NB}}(\lambda) - T_R(\lambda) \frac{t_R}{t_{\mathrm{NB}}} \frac{1}{F} \right]^{-1}, \qquad (5)$$

where $T_{\mathrm{NB}}(\lambda)$ and $T_R(\lambda)$ are the transmissions at wavelength λ for the narrowband and R filter, respectively; t_{NB} and t_R are the exposure times in the narrowband and R filters; and F is the multiplicative factor by which the R band image is scaled down to the continuum level of the narrowband image during our narrowband image continuum subtraction process. We incorporated our uncertainty in measuring F into our uncertainty in $f_{\mathrm{H}\alpha+[\mathrm{N\,II}]}$ using techniques similar to those described in Spector et al. (2012). The first term within the square brackets in

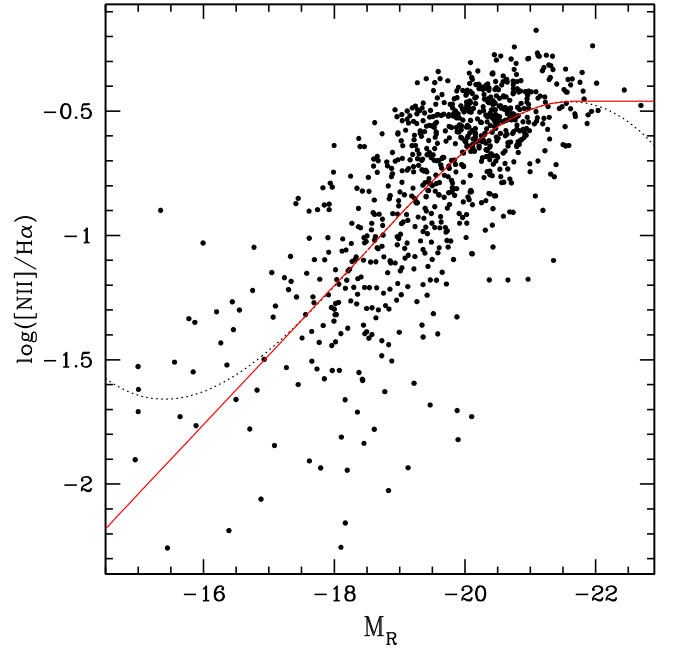**Figure 10.** The relation between the [N II]λ6583 to Hα ratio and the absolute R-band magnitude for emission line galaxies in the KISS sample. The KISS data shown has typical errors on [N II]λ6583/Hα of less than 5%. The third order polynomial fit to the data is shown as the dotted black line and our adopted fit is shown as the solid red line. We adopt this fit to statistically subtract the [N II] doublet emission that lies within our narrowband filter.

Equation (5) accounts for the wavelength dependence in the transmission of the Hα filter and the second term corrects for the Hα emission present within the R band filter. To determine the transmission values we interpolated the published filter tracings for our filters to derive a transmission at each relevant wavelength.

3.3.2. [N II] Doublet Correction

Because we do not have spectra for our galaxies, we do not know the strengths of the [N II] emission lines that fall within our narrowband filters and must utilize a statistical correction to correct for the [N II] flux. We use a sample of 803 galaxies taken from the KPNO International Spectroscopic Survey (KISS; Salzer et al. 2000, 2001; Gronwall et al. 2004a; Jangren et al. 2005a) that are known to be star-forming galaxies and which have high quality follow-up spectra (Wegner et al. 2003; Gronwall et al. 2004b; Jangren et al. 2005b; Salzer et al. 2005). Following Kennicutt et al. (2008), we develop a correlation between R-band absolute magnitude and [N II]λ6584/Hα (i.e., $f_{[\mathrm{N\,II}]\lambda6584}/f_{\mathrm{H}\alpha}$). While the current study provides accurate R-band absolute magnitudes, the KISS database does not. We used Century Survey (Geller et al. 1997) data for galaxies in common with the KISS survey to develop a relation between KISS V and $B-V$ values and Century Survey R magnitudes. Figure 10 shows the distribution of [N II]λ6584/Hα for the KISS galaxies as a function of the derived absolute R-band magnitude. We performed a variety of polynomial fits on these data to derive a relationship between M_R and $f_{[\mathrm{N\,II}]\lambda6584}/f_{\mathrm{H}\alpha}$. We concluded that the third order polynomial best fit the data, especially for high-luminosity galaxies, which are the largest contributors to our final SFRD. The original cubic fit is shown in gray in Figure 10. It is obvious that the cubic fit results in

unphysical values at both low and high luminosities, therefore we modify the original fit for absolute R-band magnitudes fainter than -18.5 and brighter than -21.6. At the low-luminosity end, we continued the almost-linear portion of the cubic fit as a line below $M_R = -18.5$. This prevents the final function from producing unphysically high [N II]$\lambda6584$/Hα values at $M_R > -17.5$. At high luminosities, the cubic function begins to become unphysical at $M_R < -21.6$, therefore we set [N II]$\lambda6584$/Hα to the maximum value of the original order three polynomial for luminosities brighter than $M_R = -21.6$. Our adopted fit is shown in red in Figure 10 and is described by

$$\log\left(\frac{f_{[\text{N II}]\lambda6584}}{f_{\text{H}\alpha}}\right) = \begin{cases} -0.279M_R - 6.231 & \text{if } M_R > -18.5 \\ 0.010M_R^3 + 0.556M_R^2 + 10.002M_R + 57.068 \\ \quad \text{if } -21.6 \leqslant M_R \leqslant -18.5 \\ -0.462 & \text{if } M_R < -21.6. \end{cases} \quad (6)$$

We adopt an error of 0.24, corresponding to the rms scatter of our cubic fit.

Using the [N II] line transmissions derived by interpolating our filter tracings, we determine the total [N II] to Hα flux ratio for each galaxy:

$$\frac{f_{[\text{N II}]\lambda\lambda6584,6548}}{f_{\text{H}\alpha}} = \frac{f_{[\text{N II}]\lambda6584}}{f_{\text{H}\alpha}}\frac{T_{\lambda6584}}{T_{\text{H}\alpha}} + \frac{1}{3}\frac{f_{[\text{N II}]\lambda6584}}{f_{\text{H}\alpha}}\frac{T_{\lambda6548}}{T_{\text{H}\alpha}}, \quad (7)$$

where $T_{\lambda6584}$, $T_{\lambda6548}$, and $T_{\text{H}\alpha}$, are the filter transmissions at the redshifted wavelength of the [N II] and Hα lines, $\frac{f_{[\text{N II}]\lambda6584}}{f_{\text{H}\alpha}}$ comes directly from Equation (6), and we assume that the strength of the [N II]$\lambda6548$ line is 1/3 the strength of the [N II]$\lambda6584$ line (i.e., in proportion to the ratio of their collision strengths; Osterbrock & Ferland 2006). We can then determine the corrected flux:

$$f_{\text{H}\alpha,\text{corr}} = \frac{f_{\text{H}\alpha+[\text{N II}]}}{\left(1 + \frac{f_{[\text{N II}]\lambda\lambda6584,6548}}{f_{\text{H}\alpha}}\right)}, \quad (8)$$

where $f_{\text{H}\alpha+[\text{N II}]}$ comes from Equation (5).

3.3.3. Dust Corrections

The ALFALFA Hα sample, by design, avoids the plane of the Galaxy, but we still must correct for absorption due to foreground dust in the Milky Way. To do this we used the $E(B-V)$ reddening values derived from the Schlafly & Finkbeiner (2011) recalibration of the Schlegel et al. (1998) extinction maps. To compile these values, we used the NED coordinate and extinction calculator to find the total absorption (A_λ) in both the B band and the V band. We assume an $R_V = 3.1$ absorption law, $A_B = 4.3\ E(B-V)$, and use reddening function values from Osterbrock & Ferland (2006) resulting in a flux correction

$$f_{\text{H}\alpha,\text{Gcorr}} = f_{\text{H}\alpha,\text{corr}}10^{0.818A_B/2.9}. \quad (9)$$

In addition to Galactic absorption and [N II] contamination, the observed Hα flux is also extincted by the dust in the host galaxy. To correct for this internal absorption, we again use the same sample of KISS emission line galaxies that we used for our [N II] line flux correction to derive a statistical correction.
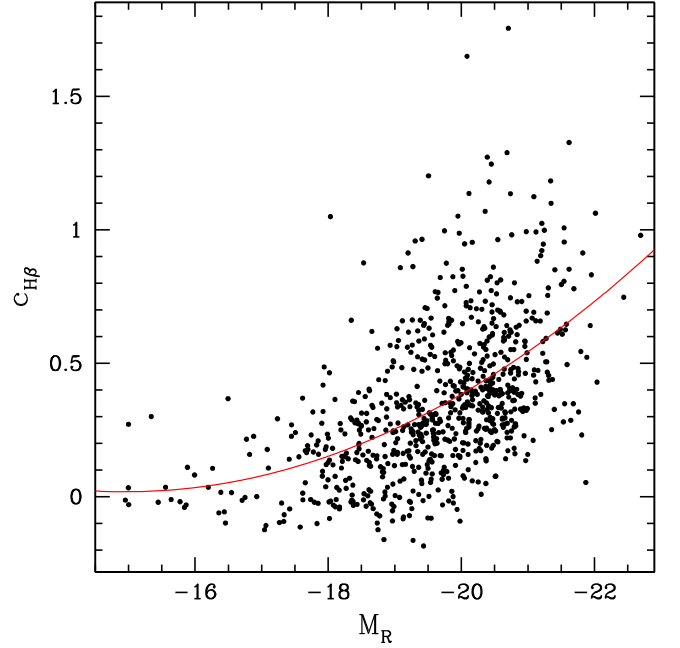

Figure 11. The relation between $c_{\text{H}\beta}$ and the absolute R-band magnitude for emission line galaxies in the KISS sample. The $c_{\text{H}\beta}$ values determined by KISS have errors well below 0.2 dex, with typical errors close to 0.1 dex. The second order polynomial fit is shown as the solid red line. We use this fit to determine internal absorption corrections for our galaxies.

Figure 11 shows the relationship between $c_{\text{H}\beta}$ and M_R for the KISS sample of galaxies, where the values for $c_{\text{H}\beta}$ are derived from the galaxy spectra using the ratio $f_{\text{H}\alpha}/f_{\text{H}\beta}$. For each galaxy we adopt the $c_{\text{H}\beta}$ value corresponding to the derived R-band absolute magnitude based on the the polynomial fit shown in red in Figure 11:

$$c_{\text{H}\beta} = 0.014M_R^2 + 0.430M_R + 3.233. \quad (10)$$

We adopt a constant uncertainty of 0.23, corresponding to the rms scatter of the data. Assuming the same reddening function as for the Galactic absorption correction our flux correction is

$$f_{\text{H}\alpha,\text{gcorr}} = f_{\text{H}\alpha,\text{Gcorr}}10^{0.818c_{\text{H}\beta}}. \quad (11)$$

3.3.4. Internal Dust Absorption Comparison

The correction for internal absorption can be large and ultimately will directly impact the determination of the SFRD. Hence, it is useful to be able to check the validity of our applied correction using an alternate and completely independent method. Our internal absorption correction is a statistical correction; the KISS and ALFALFA Hα samples do not overlap, so we have no uniform direct spectroscopic data set for our galaxies. The WISE all-sky survey area (Wright et al. 2010) and our survey area do overlap, so we can directly compare WISE-based internal absorption corrections to our statistical correction (derived using the KISS spectroscopic data) for ALFALFA Hα galaxies that have WISE data.

We searched the WISE database for detections within 6″ (the resolution of the WISE 3.4 μm, W1 band) of the ALFALFA optical coordinates. Out of our 565 Fall sample galaxies, 367 have WISE measurements in the W3 (12 μm) band, the W4 (22 μm) band, or both. We applied the corrections described in Jarrett et al. (2013) to the WISE data. We then used our derived
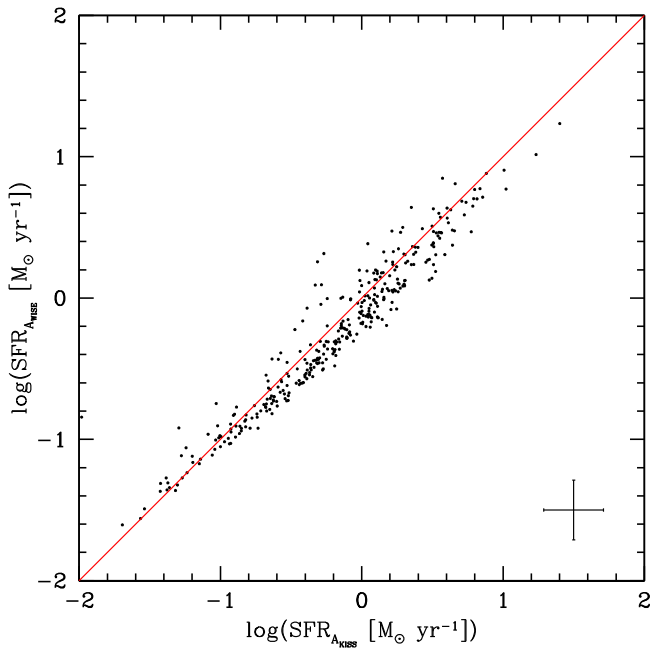
Figure 12. A comparison of our SFRs derived using a statistical internal absorption correction derived from a KISS spectroscopic data set, and SFRs derived using an internal absorption correction based on *WISE* using the *WISE* W3 (12 μm) band data. We show a representative error bar in the bottom right.

WISE luminosities in the *W*3 and *W*4 bands and our Hα luminosities (uncorrected for internal absorption) to determine the SFR based on the prescriptions given in Wen et al. (2014). We also applied a correction factor of 1.473 to the Wen et al. (2014) SFRs to convert from their SFR calibration to our Kennicutt (1998) calibration. This comparison and analysis is described in Jaskot et al. (2015), as it was first used in their work with starburst galaxies in the Fall ALFALFA Hα sample.

Figure 12 shows the comparison of our final SFRs, which were derived with the internal absorption correction described in Section 3.3.3 to the SFRs we derived following Wen et al. (2014). The SFRs derived using the two distinct absorption corrections agree with each other reasonably well, although the scatter is significant. The *WISE*-based method tends to give slightly lower SFRs for the galaxies with SFRs around $1\,M_\odot\,\mathrm{yr}^{-1}$. The median offset between the two methods is 0.09 dex, although above $\log(\mathrm{SFR}\,[M_\odot\,\mathrm{yr}^{-1}]) = -0.4$ it is 0.12 while below this SFR it is 0.04 dex.

Figure 12 is an illustration of how different methods for estimating the absorption in galaxies can have a significant effect on SFRs and therefore our final SFRD. We choose to use the spectroscopic KISS data to define our internal absorption corrections because not all of our galaxies have data in the *WISE* catalog and therefore would not have an absorption correction based on the Wen et al. (2014) method. We discuss the systematic effects of different choices of internal extinction correction on the SFRD in Section 5.2.

4. SFRD MEASUREMENT

For each galaxy in our sample, we calculate an SFR using the Hα luminosity corrected for Galactic and internal extinction and [N II] contamination. We adopt a conversion that is derived

using the relations in Kennicutt (1998) with a Salpeter IMF:

$$\mathrm{SFR} = \frac{L_{\mathrm{H}\alpha}}{7.9 \times 10^{42}}, \tag{12}$$

where SFR is in $M_\odot\,\mathrm{yr}^{-1}$ and $L_{\mathrm{H}\alpha}$ is the Hα luminosity in erg s^{-1} determined using

$$L_{\mathrm{H}\alpha} = 4\pi D^2 f_{\mathrm{H}\alpha,\mathrm{gcorr}}, \tag{13}$$

where D is the distance from the α.40 catalog and $f_{\mathrm{H}\alpha,\mathrm{gcorr}}$ is from Equation (11). The conversion of Hα luminosity to SFR makes several standard assumptions, including the use of the Salpeter (1955) IMF and solar metallicities. The ALFALFA team derived distances for all of their extragalactic sources using a flow model and assuming a Hubble constant of $H_o = 70\,\mathrm{km\,s}^{-1}\,\mathrm{Mpc}^{-1}$. We adopt these distances provided in the α.40 catalog for our sample in order to derive all distance-dependent properties.

Additionally, because Equation (12) assumes only thermal emission (the majority of which originates from OB stars), we examine the level of AGNs contamination present in each of our samples. To do this we search the catalog compiled by Véron-Cetty & Véron (2010) for any galaxies included in our volume. Véron-Cetty & Véron (2010) contains all AGNs with magnitudes brighter than $M_B = -22.25$ (and many with lower luminosities) known as of 2009 July 1. We eliminated the contamination from AGNs by subtracting the flux coming from the nuclear region from the total measured narrowband flux of the host galaxy. We do not include any additional corrections for AGN contamination in our SFRD calculations.

In this section, we outline our method for calculating the local SFRD. The majority of our methods used to calculate the SFRD do not depend on the particular sub-sample we are using to determine the SFRD. The details of the methods or corrections that are sample-dependent are presented separately. The presentation of the local SFRD measurement using our Fall sample and the quantitative details of our corrections and measurements are presented in Section 5. Our forthcoming Paper 3 will include a measurement of the local SFRD based on our Spring sample.

4.1. Incompleteness Corrections

4.1.1. $1/V_{\mathrm{max}}$ Correction

Though our survey includes all of the ALFALFA targets in a fixed volume, the ALFALFA survey itself is an H I-flux-limited sample. Therefore, we must apply a completeness correction to our sample that accounts for the selection function derived by the ALFALFA team. The ALFALFA selection function depends on the velocity width at half maximum (W_{50}), as well as the integrated line flux (S_{21}). The 90% completeness limit quoted in Haynes et al. (2011) is

$$\begin{aligned} &\log S_{21,90\%} \\ &= \begin{cases} 0.5\log W_{50} - 1.11 & \text{if } \log W_{50} < 2.5 \\ \log W_{50} - 2.36 & \text{if } \log W_{50} \geqslant 2.5, \end{cases} \end{aligned} \tag{14}$$

$$\log S_{21,90\%,\mathrm{code}\,1} = \log S_{21,90\%} + 0.033. \tag{15}$$

The selection function is determined by the ALFALFA team for both code 1 and 2 objects (Equation (14)), and also for only code 1 objects (Equation (15)) because of possible bias due to the nature of the code 2 sample (see Section 2). To derive their

completeness limits, Haynes et al. (2011) plot the observed $S_{21}^{3/2} \frac{dN}{d \log S_{21}}$ versus S_{21} for multiple bins in $\log W_{50}$. $S_{21}^{3/2} \frac{dN}{d \log S_{21}}$ will be constant if there is no incompleteness. They then fit an error function to the data to determine 90%, 50%, and 25% completeness limits. In practice, these limits are constant offsets in $\log S_{21}$ from each other. We extended this completeness analysis to derive a "100%" completeness limit:

$$\log S_{21,100\%} = \log S_{21,90\%} + 0.028, \qquad (16)$$

which we derived by continuing the linear relation between the completeness limit and the constant offset.

We use this selection function to derive a weight which we apply to each galaxy in our sample. We determine the maximum volume within which each galaxy could be detected by ALFALFA, V_{max}, and apply a weight to each galaxy. If V_{max} is greater than V_{survey} (the volume of our survey), the galaxy can be detected throughout the survey volume, and the weighting factor is set to 1, otherwise we apply a weight of V_{survey}/V_{max}. With this method, the lowest mass galaxies, which are not detected in our entire survey volume, are given a weight that is greater than 1, while galaxies that are detected throughout our volume are given a weight of 1. This correction is only valid for galaxies that ALFALFA detected within our survey volume.

For H I masses above $\sim 10^{9.3} M_\odot$, ALFALFA is 100% complete within our survey volume. This means that $\sim 34\%$ of our target galaxies have H I masses that are detectable throughout the ALFALFA Hα volume.

4.1.2. Inner Distance Limit Correction

Our $1/V_{max}$ incompleteness correction accounts for galaxies that have the potential to be detected by ALFALFA within our survey volume. However, it does not account for low H I-mass galaxies that are missing from our sample due to our inner velocity limit. Galaxies with H I masses below $\sim 3 \times 10^7$ are detected by ALFALFA, but are excluded from our sample because they are only detected by ALFALFA at velocities lower than our survey limit (1460 km s^{-1}; ~ 20 Mpc). A separate correction is needed for these low H I-mass galaxies. This type of correction is not typically used when calculating the SFRD, but our sample construction requires it. We choose to test the effect of including this correction to assure that we are accounting for *all* missing galaxies, even galaxies below the detection limit of ALFALFA in our survey volume, that may be forming stars.

To do this we utilize the Schechter function parameters for the HIMF derived from the ALFALFA α.40 sample (Martin et al. 2010): $\theta^* = 0.0048 \pm 0.0003$, $\log(M^*/M_\odot) = 9.96 \pm 0.02$, and $\alpha = -1.33 \pm 0.02$. We then choose some H I mass, $M_{H\,I,cut}$, above which we sum our observed, weighted SFRs and below which we integrate

$$\text{SFR}_{tot}(M_{H\,I}) \cdot dM_{H\,I} = \theta^* \cdot (M_{H\,I}/M^*)^\alpha \cdot e^{-M_{H\,I}/M^*}$$
$$\cdot \text{SFR}(M_{H\,I}) \cdot d(M_{H\,I}/M_*) \qquad (17)$$

to determine the amount of SF below $M_{H\,I,cut}$. Our choice of appropriate $M_{H\,I,cut}$ is specific to our sample, so further details are discussed in Section 5 for the Fall sample and in Paper 3 for the Spring sample. We derive the function SFR($M_{H\,I}$) by fitting a broken power law to our data from both our Fall and Spring
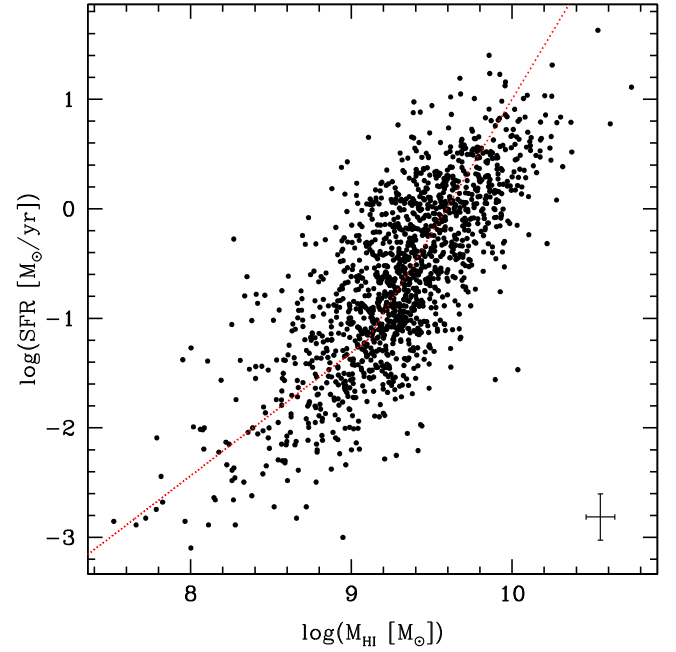

Figure 13. The black points show the SFRs of the entire ALFALFA Hα sample as a function of H I mass. We show a representative error bar in the lower right. The red line is our fit to the data. We use this SFR($M_{H\,I}$) function to determine the integrated SFR contributed by the galaxies with the lowest H I masses, which includes galaxies that fall below ALFALFA's detection limit at our inner distance limit.

samples. Our fit is shown in Figure 13 as a red line:

$$\log\left(\frac{\text{SFR}}{M_\odot \, \text{yr}^{-1}}\right)$$
$$= \begin{cases} 1.125 \cdot \log\left(\frac{M_{H\,I}}{M_\odot}\right) - 11.438 & \text{if } \log\left(\frac{M_{H\,I}}{M_\odot}\right) \leqslant 9.1 \\ 2.444 \cdot \log\left(\frac{M_{H\,I}}{M_\odot}\right) - 23.444 & \text{if } \log\left(\frac{M_{H\,I}}{M_\odot}\right) > 9.1. \end{cases}$$
$$(18)$$

To calculate our total SFRD, we use the HIMF-determined SFR contributed by galaxies with masses lower than $M_{H\,I,cut}$ and add it to our data-determined SFR contributed by galaxies with H I masses higher than $M_{H\,I,cut}$ then divide by the geometric volume of our survey. In practice, this correction is negligible, but we have included a discussion of it here for completeness.

4.2. Large-Scale Structure Correction

In addition to applying completeness corrections when we calculate our SFRD, we must also ensure that we are sampling a typical volume of the universe. This, like our inner distance limit correction, is not typically done when calculating SFRD. However, it is important to quantitatively measure whether our sample contains a representative range of environments and to apply a correction if our sample over-selects galaxies in either high- or low-density environments. This is especially important in our study because high- and low-density environments are known to preferentially contain elliptical and star-forming galaxies, respectively (e.g., Dressler 1980; Binggeli et al. 1988). This correction is different for each of our two sky samples. We discuss the details of this correction that are

unique for the Fall sample in Section 5 and for the Spring sample in Paper 3. Here we give an overview of the correction method.

To make sure we are sampling a representative volume of the universe, we compare the volume densities of our Fall and Spring samples to a larger volume that is presumably a representative sample of the overall galaxy distribution. Then we apply a correction to our final SFRD based on the number densities of galaxies in both volumes,

$$\text{SFRD}_{\text{corr}} = \text{SFRD} \cdot n_{\text{comparison}}/n_{\text{Sample}}, \qquad (19)$$

where $n_{\text{comparison}}$ is the number density of the comparison sample and n_{Sample} is the number density of galaxies in either our Fall or Spring sample.

Using an optically selected data set for comparison would sample a different density distribution (i.e., more high-density environments) than that in which H I-selected galaxies reside. Because of this, we decided to compare our sample to a larger H I-selected sample. The most appropriate comparison sample for us to use is the ALFALFA sample itself. Therefore, we constructed our comparison sample from the α.40 catalog utilizing the entire sky coverage area, both in the fall and spring skies, between our inner velocity limit and 9500 km s^{-1}. Both our Fall and Spring volumes lie within this volume. Therefore, we excluded the ALFALFA Hα Fall volume from our comparison sample when calculating the correction to the Fall SFRD, and likewise excluded the Spring volume when determining the correction to the Spring SFRD. In all cases, we excluded the Virgo cluster region because it is a known density enhancement. Additionally, by using the same inner velocity limit as our Fall sample, we are also excluding the Local Supercluster from our comparison volume. Our resulting comparison volumes are ~17 times larger than our Fall volume and ~7 times larger than our Spring volume. Galaxies with H I masses of $M_{\text{H I}} \geqslant 10^{9.66} M_\odot$ can be detected within our entire comparison volume, so these are the galaxies that we use to determine number densities in both our comparison volume and our sample volumes. Our final $n_{\text{comparison}}/n_{\text{Sample}}$ will not change with the H I mass limit we use, assuming the HIMF is the same in our comparison and sample volumes. We arrived at our minimum mass of $M_{\text{H I}} = 10^{9.66} M_\odot$ after iterating through different mass and velocity limits. This minimum mass is far enough below the knee in the HIMF ($10^{9.96} M_\odot$, as determined by the ALFALFA team) to allow for sufficient numbers of galaxies in both our comparison and sample volumes and our velocity limit is high enough to cover a full range of environmental densities. This LSS correction turns out to be small for our Fall volume. That is, $n_{\text{comparison}}/n_{\text{Sample}}$ is close to unity. This means that the volume covered by the Fall ALFALFA Hα sample is very close to a fair representation of the local universe.

5. A PRELIMINARY ESTIMATE OF THE LOCAL SFRD

To demonstrate how different galaxy samples (i.e., code 1 and 2 sources, OTHERs) and each of our corrections affects the SFRD, we include Table 2. The first column of Table 2 labels which correction or corrections were applied to the SFRD in that row. The first row is labeled "None" (i.e., no correction) and is simply the sum of the SFRs divided by the Fall volume. Each of the subsequent rows shows the result of incorporating an additional correction. The second column contains SFRD values that result from using *only* code 1 sources, whereas the

Table 2
log(SFRD[$M_\odot$ yr^{-1} Mpc^{-3}])

	log(SFRD[$M_\odot$ yr^{-1} Mpc^{-3}])	
Correction	Code 1	Code 1 and 2
None	$-1.900^{+0.020}_{-0.022}$	$-1.887^{+0.020}_{-0.021}$
$+V_{\text{max}}$	$-1.781^{+0.018}_{-0.019}$	$-1.768^{+0.018}_{-0.019}$
$+$LSS	$-1.760^{+0.018}_{-0.019}$	$-1.747^{+0.018}_{-0.019}$
$+$OTHERs	$-1.747^{+0.018}_{-0.018}$	$-1.735^{+0.017}_{-0.018}$

Note. A summary of our SFRD measurements after each correction is applied. We divide our sample into all galaxies (code 1 and 2) and just code 1 galaxies. We also show the effect of including the emission from the OTHERs. Our quoted values are in units of log($M_\odot$ yr^{-1} Mpc^{-3}).

third column shows the SFRD incorporating all ALFALFA sources. Each correction (i.e., row in Table 2) is described below. We discuss both the systematic and random errors associated with these corrections in Section 5.2.

5.1. The Local SFRD from the Fall Sample

Of the 565 galaxies in our Fall sample, 542 are detected in Hα. We use these 542 galaxies and 101 OTHERs to calculate the local SFRD. All of the corrections described in Section 3.3 are applied to the flux of each galaxy. Additionally, only one of the 565 galaxies in our Fall sample contains a known AGN. The galaxy is UGC 1479 and is classified as a type 2 Seyfert galaxy by Gallego et al. (1997) as part of the Universidad Complutense de Madrid objective prism survey. UGC 1479 does exhibit point-like Hα emission from its nucleus, in addition to extended emission located in the disk of the galaxy. We describe how we correct the flux for the presence of an AGN in Section 4. For UGC 1479, the AGN contributes ~9% of the total Hα flux from the galaxy.

Below, we describe how we correct the Fall sample for incompleteness, account for any biases our sample may have in terms of galaxy number density, and examine the effects code 2 sources (see Section 2.1) and OTHERs (see Section 3.2) have on our final SFRD. Section 4.1 describes our methods for each of the corrections we make to the SFRD.

The $1/V_{\text{max}}$ correction affects a significant fraction of our Fall sample galaxies. Only 207 of the 542 galaxies (38%) are detectable in H I throughout our entire sample volume. However, these are the more massive galaxies that contribute 72% of the total SF in our survey volume. The remaining 335 galaxies all require some level of correction to account for incompleteness. This correction is the largest that we apply to our Fall sample. Including this correction increases the SFRD by ~30% (see the row labeled "V_{max}" in Table 2).

Using our empirical fit for SFR($M_{\text{H I}}$) (Figure 13), we explore how our choice of $M_{\text{H I,cut}}$ (see Section 4.1.2) would affect our final SFRD. Figure 14 illustrates how our derived SFRD changes with our choice of $M_{\text{H I,cut}}$. Total SFRDs are shown in black and the contribution to these SFRDs from our observations (i.e., galaxies with masses above $M_{\text{H I,cut}}$) are shown in green. The difference between the black and green points is therefore the contribution to the SFRDs from our integration of Equation (17) below $M_{\text{H I,cut}}$. The SFRs from our observations include our $1/V_{\text{max}}$ correction. It is clear that the galaxies with the highest H I masses (i.e., those with masses above $M_{\text{H I,cut}}$) contribute the most to the SFRD. We have also included our formal uncertainties for the $1/V_{\text{max}}$ estimate of the local SFRD in Figure 14 represented by the red dotted lines.
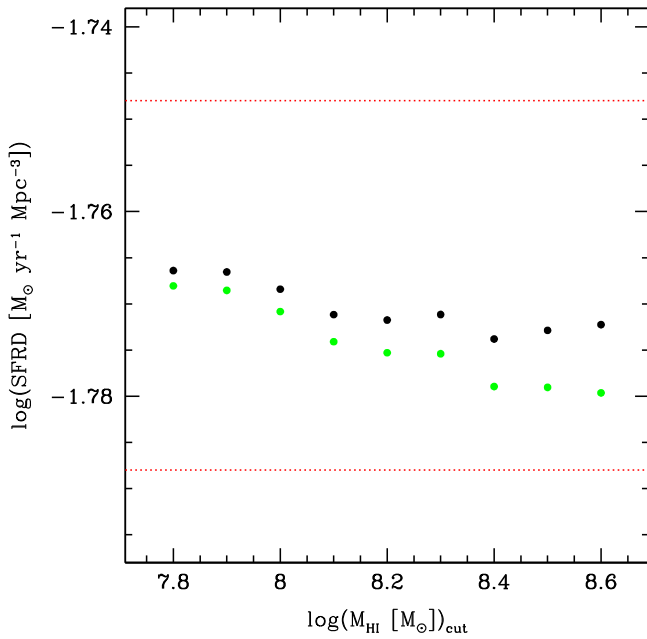
Figure 14. Our total SFR densities (black) and the contribution to the SFRD by H I masses greater than $M_{\rm H\,I,cut}$, the mass below which we use only the HIMF and our empirical SFR($M_{\rm H\,I}$) to determine the SFRD (green). All points lie within the error bars of our SFRD estimate (shown as red dotted lines), indicating that the value of $M_{\rm H\,I,cut}$ adopted makes little difference.

All of our total SFRD points, *regardless* of $M_{\rm H\,I,cut}$, lie well within our shown error bars. This indicates that our final SFRD is essentially independent of our choice of $M_{\rm H\,I,cut}$. This analysis also shows that the SFRD is the same, within the errors, as our SFRD using only the $1/V_{\rm max}$ correction.

The resulting SFRD does not increase when we include the HIMF correction, as would be expected if we had missed a significant amount of SF due to our inner distance limit. Therefore, we conclude that this correction does not add any information to our final SFRD and choose to exclude it.

For our LSS correction, galaxies with masses above $M_{\rm H\,I} = 10^{9.66}\,M_{\odot}$ are detected throughout the comparison volume and are used to determine number densities in both our comparison volume and our Fall volume. Our resulting comparison volume is ∼17 times larger than our Fall volume.

To determine the volume and the number of galaxies within that volume we used CMB rest-frame velocities instead of the heliocentric velocities quoted in the $\alpha.40$ catalog. Because of this velocity conversion, the inner velocity limit becomes $1187\,\mathrm{km\,s^{-1}}$. After measuring the number densities of galaxies in the comparison and Fall volumes, we find a correction factor for code 1 objects of $n_{\rm comparison}/n_{\rm Fall} = 1.0482 \pm 0.0009$, which indicates that our volume is slightly under-dense, but very close to being a representative sample of environmental densities.

This LSS correction is small, which was one of our intentions when designing this survey. If we had not expanded our sample and only used Phase I galaxies, we would have had a slightly over-dense sample and our correction factor would have been $n_{\rm comparison}/n_{\rm Fall} = 0.918 \pm 0.004$. By expanding our sample to include our Phase II sample, we improved our sampling of environmental densities, which was one of the primary purposes of the survey expansion. This correction affects our SFRD within our statistical error bars. Our SFRD

increases by ∼0.021 dex when we include this correction (see the row labeled "LSS" in Table 2).

In Table 2, the row labeled "OTHERs" shows the SFRD when OTHERs are included in the calculation. All OTHERs are used in the "code 1 and 2" calculation, however only OTHERs which are associated with code 1 targets are included in the code 1 calculation. Incorporating the OTHERs into our SFRD calculation results in a systematically higher SFRD. The SFRD increases by ∼3% when we include OTHERs in the calculation, which emphasizes that the vast majority of SF in our volume occurs within our target galaxies.

Table 2 also shows the effect of code 2 objects on our final SFRD. Only 17 target galaxies in the Fall sample have code 2 designations. The SFRD calculated using only code 1 sources is systematically lower than the SFRD calculated using all galaxies. The effect of code 2 sources on our Fall SFRD is discussed in Section 5.2. For the Fall sample, the systematic offset between SFRDs calculated using code 1 and 2 sources and using only code 1 sources is smaller than our random error bars, so this effect is small. Nonetheless, we adopt the SFRD that includes only code 1 sources as well as their associated OTHERs: $\log({\rm SFRD}/[M_{\odot}\,{\rm yr^{-1}\,Mpc^{-3}}]) = 1.747 \pm 0.018$ (random) ± 0.05 (systematic).

5.2. Discussion of Errors

5.2.1. Random Errors

We propagate our random errors through all stages of our analysis. In our calculation of SFRs, we include uncertainties in the instrumental magnitudes, photometric zero points, continuum estimation (e.g., Spector et al. 2012), H I masses, and distances as well as the errors on the fits used to derive the corrections for [N II] contamination and internal extinction. Each of our corrections applied to our SFRD (e.g., $1/V_{\rm max}$ and LSS corrections) has an associated uncertainty, which we include in our analysis as well.

Our consistent observing procedures, image processing, and aperture photometry, combined with the excellent depth of our data, help to keep our photometric errors small. A more complete discussion of the errors associated with our photometry, including instrumental magnitudes, photometric zero points, and continuum measurements, will be discussed in Paper 2. Here, we describe the magnitude of the errors that contribute to the error on our calibrated fluxes. Our measured instrumental magnitudes typically have errors of <4%. As discussed in Section 3.1, we used a set of four spectro-photometric standard stars to determine our zero points. The errors on our nightly zero points are typically less than 0.01 mag. We use the error on the scale factor applied to the R band image during continuum subtraction (F in Equation (5)) to characterize the error on our continuum measurement. We use a method similar to that described by Spector et al. (2012) to calculate the error on our continuum measurement assuming a representative 0.1 error on F, which results in an error contribution of less than 1% of our derived Hα+[N II] flux. The resulting calibrated fluxes from our observations typically have errors of <5%.

We adopt the H I masses and distances quoted in the $\alpha.40$ catalog (Haynes et al. 2011). The catalog includes the formal uncertainty in the H I mass of each galaxy, but it does not include an estimate of the uncertainty in the distance. The ALFALFA team used a flow model (Masters 2005) to

determine distances to H I sources based on their observed positions and CMB rest-frame recession velocities. This model produces distances with uncertainties of 10%, therefore we adopt a 10% error on galaxy distance with a minimum error corresponding to the mean velocity dispersion of the model, $163 \, \mathrm{km \, s^{-1}}$. The error on the distance dominates the random error in our luminosities and therefore in the SFRD.

The uncertainties associated with our adopted values for our two statistical corrections for [N II] contamination and internal extinction are discussed in Section 3.3, where we also derive these corrections. In both instances we use the root mean squared scatter of the data about the fits to define our random errors. For both corrections we adopted a constant uncertainty. These uncertainties are small compared to the uncertainty on the distance but we include them at all points of our analysis.

The completeness correction and our LSS correction both have uncertainties associated with them. The uncertainties in the $1/V_{\mathrm{max}}$ correction depend on the error in the H I mass as well as the error in distance. Because the distance to an individual galaxy has an uncertainty, so too does our error on the corresponding V_{max} and we take this uncertainty into account when calculating the correction for each galaxy.

Our sample also requires a correction that accounts for any bias due to LSS. This correction utilizes number densities when comparing our volume to a comparison volume. The uncertainty in this correction is due to Poisson statistics, and because our Fall and comparison samples are large, the relative error is correspondingly small.

5.2.2. Systematic Errors

There are several possible sources of systematic error in our SFRD analysis. Our choice of distance model (H_0), initial mass function, reddening function, [N II] contamination estimation, internal extinction estimation, and use of code 2 objects all have systematic effects on our measurement of the local SFRD. We have adopted the same Hubble constant assumed by the ALFALFA team. To estimate the systematic uncertainty associated with this assumption, we calculate the SFRD using both $H_0 = 68$ and $70 \, \mathrm{km \, s^{-1} \, Mpc^{-3}}$ and adopt the difference of 0.02 dex as the uncertainty. These two values of H_0 are intended to represent the range of current estimates of the Hubble constant (e.g., Bennett et al. 2013; Planck Collaboration et al. 2014).

Our choice of initial mass function used for the conversion from Hα luminosity to SFR affects our final SFRD in a very predictable way. If we adopt an alternate initial mass function, our SFRD will be offset by some multiplicative factor (an additive constant in the log). This systematic is relatively simple to account for when comparing with other measurements, but if unaccounted for, can contribute a systematic difference up to ~0.4 dex. Because we account for this systematic when comparing our value to others, we do not include it in our quoted systematic error.

The choice of reddening function can significantly affect the SFRD. To estimate the magnitude of the effect this parameter has on our measurement of the local SFRD we calculate the SFRD using a Small Magellanic Cloud-like extinction function (Osterbrock & Ferland 2006). We then compare the resulting SFRD to the SFRD calculated using the extinction law we assume throughout this paper ($R_V = 3.1$) and adopt the difference, 0.02 dex, as our systematic uncertainty.

We also examined the two statistical corrections we apply to our data to correct for [N II] contamination and internal extinction. To investigate these corrections, we created a large number (10,000) of artificial samples selected from the empirical distribution of the KISS data we used to derive our [N II] and internal extinction corrections. We used the resulting bootstrap resampling distribution of SFRDs for two purposes: to establish fits that represent the empirical distribution and to determine if either correction introduces a systematic bias to our SFRD estimate. The fits described in Section 3.3 are the result of testing numerous fitting functions and methods. The SFRD distributions resulting from our bootstrap resampling distributions are well represented by our final fits quoted in Equations (6) and (10). We also found that using our fit for the [N II] correction did not introduce any systematic error in our final SFRD. However, the medians of the SFRD distributions produced by our internal extinction fit and our resampling method are offset by 0.04 dex. Therefore, we include a systematic uncertainty of 0.04 dex, which can be introduced by the internal extinction correction we adopt (i.e., Equation (10)).

Our final source of systematic error is introduced by using code 2 sources. Code 2 objects are included in the published ALFALFA database if there exist optical data that coincide with the location and redshift of the ALFALFA detection (see Section 2.1). Introducing objects that require an optical "prior" will likely introduce a small bias into our sample. We estimate the magnitude of this error empirically by comparing SFRD values that incorporate code 2 sources with those that exclude theses sources. As can be seen in Table 2, the difference is within, but similar in size to our random error bars for our Fall sample. As we describe in Section 5, we adopt a SFRD for our Fall sample that excludes code 2 sources, so this error does not contribute to our quoted systematic error bars.

In our discussion of how our measurement of the local SFRD compares to other measurements, all of the literature SFRD values are scaled to a common (Salpeter) IMF and the cosmology we have assumed throughout this paper. We include the errors introduced by the IMF and Hubble constant in our discussion of systematic errors for completeness, however, we do not include these as part of our total systematic error because we have corrected for them in our comparison. Additionally, as discussed above and in Section 5, we do not include an estimate of the systematic error introduced by code 2 sources in our total systematic error, rather we exclude the sources from our adopted SFRD. Under the assumption that our remaining systematic errors are uncorrelated, we adopt a total systematic error of 0.05 dex.

6. DISCUSSION

6.1. Comparison of SFRD to Literature

There are several measurements of the local SFRD in the literature that utilize Hα emission to measure the SFR in each galaxy (Gallego et al. 1995; Tresse & Maddox 1998; Sullivan et al. 2000; Perez-Gonzalez et al. 2013; Brinchmann et al. 2004; Nakamura et al. 2004; Hanish et al. 2006; James et al. 2008; Westra et al. 2010; Gunawardhana et al. 2013). To select their samples, these studies utilize a broad spectrum of techniques. For example, some use objective prism surveys designed to find Hα emission, some select galaxies based on brightness in broadband optical/UV/IR filters, and others

select galaxies based on their H I line emission in the radio. The sample sizes of these studies vary from ~80 to ~1500. Gunawardhana et al. (2013) corrected all of the SFR densities from these studies to a common cosmology and IMF (Salpeter 1955) so they could be compared. These Hα-emission-based SFRD measurements are shown in red in Figure 15 along with our SFRD measurement in black. The horizontal error bars show the redshift range of the various samples. The vertical error bars represent the random errors on each SFRD measurement. We note that the vertical error bars on our SFRD measurement are smaller than the symbol size.

Compared to the other local SFR densities measured with Hα, our SFRD is consistent with the weighted average below $z = 0.15$ ($\log(\mathrm{SFRD}/[M_\odot\ \mathrm{yr}^{-1}\ \mathrm{Mpc}^{-3}]) = -1.74^{+0.14}_{-0.20}$) and agrees with other studies, including the local SFRD derived by Hanish et al. (2006) using the SINGG sample (see Section 2.3). Some of these Hα-based studies utilized spectra to measure the Balmer decrement (Hα/Hβ, with line fluxes corrected for stellar absorption) to determine the internal extinction correction. Some used this method for some of their target galaxies, but needed to employ a constant absorption correction for galaxies without a well-measured Hβ flux. Other studies that did not have spectra of their targets used empirical fits to relationships derived from spectral survey data, or, in the case of James et al. (2008), derived their own morphology-dependent extinction correction. Both Gallego et al. (1995) and James et al. (2008) also utilized infrared data to verify their extinction corrections. The red points in Figure 15 are labeled according to the extinction correction used: spectral Balmer decrement (filled triangles), empirical fit (open triangles), or morphology-dependent (open stars). The choice of which technique to use to correct for obscured SF can significantly affect the final SFR density (see our comparison of our internal extinction correction with one based on *WISE* data in Section 3.3.4 and our discussion of systematic errors introduced by our internal extinction correction in Section 5.2). The presence of a range of internal absorption correction techniques is likely one contribution to the observed scatter in the local SFRD.

Figure 15 also shows measurements of the local SFRD using all types of SFR measures. As stated earlier, the red points show Hα-based SFR densities. SFR densities based on UV continuum emission are in blue, forbidden oxygen line emission ([O II]/[O III]) in cyan, infrared continuum emission in magenta, and radio continuum emission in green. Each of these techniques has its own advantages and limitations. The scatter present in the SFRD based on different SF indicators is similar to the scatter seen in just the Hα-based points. This suggests that sample selection biases and other inconsistencies are likely the dominant factor contributing to the scatter rather than different SFR measurement methods. Nonetheless, in the context of all SFRD measurements, our SFRD agrees with not only other Hα-based SFR densities, but multiple other measurements using each of the previously mentioned SFR detection methods. Finally, Figure 16 shows our SFRD measurement in the context of SFRD measurements throughout cosmic history (Hopkins 2004; Gunawardhana et al. 2013; Madau & Dickinson 2014, and references therein). There is a similar scatter in SFRD measurements at both local and high redshifts.

As seen in both Figures 15 and 16, our new estimate of the local SFRD has much smaller random uncertainties than the
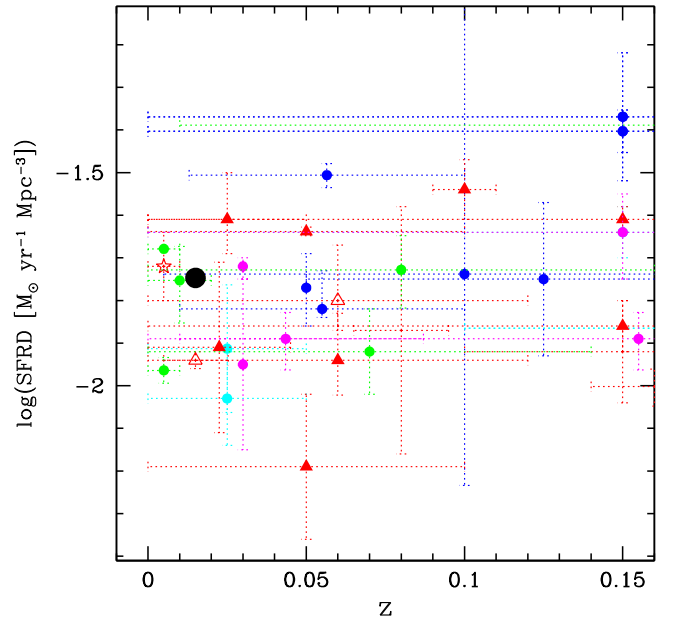

Figure 15. Local SFRD measurements. The horizontal error bars represent the redshift range of each sample and the vertical error bars represent the random error on each measurement of the SFRD. The random error bars for our measurement of the SFRD are smaller than the symbol size. The colored points are from the literature and the black point is our measurement. The different colors indicate different SFR measurement methods. red: Balmer lines (Hα/Hβ); blue: UV; cyan: Oxygen ([O II]/[O III]); magenta: IR; and green: Radio. Different symbols indicate different internal extinction correction methods for local Hα-based SFR measurements: filled triangles represent extinction corrections based on spectroscopic data of the target galaxies, open triangles empirical fits to spectroscopic data, and open stars morphology.

vast majority of the previous measurements. Our local SFRD value is slightly below—but in agreement with—the weighted average of the previous local ($z \leqslant 0.15$) SFRD measurements, $\log(\mathrm{SFRD}/[M_\odot\ \mathrm{yr}^{-1}\ \mathrm{Mpc}^{-3}]) = -1.69^{+0.16}_{-0.26}$. Our new value provides a solid anchor point with which to assess the total change in SFRs over time. Compared to the weighted average of SFRD values around $z \approx 2$, $\log(\mathrm{SFRD}/[M_\odot\ \mathrm{yr}^{-1}\ \mathrm{Mpc}^{-3}]) = -0.74 \pm 0.20$, our local value indicates a drop in the global SFRD of a factor of 10.2 over that lookback time.

6.2. Other Applications of ALFALFA Hα

While the primary goal of the ALFALFA Hα survey is to produce the definitive measurement of the local SFRD, this result will by no means be all that we will accomplish with these data. Our large sample of Hα and broadband *R* images has multiple additional uses. Here, we emphasize the versatility of our data set by describing several ongoing or future planned projects that utilize our data set.

H I properties of starburst galaxies: Jaskot et al. (2015) use the Fall ALFALFA Hα data set to investigate the H I and star-forming properties in a sample of starbursting galaxies. This project explores accretion and feedback in these systems, including their effect on H I content and the role these processes play in triggering and sustaining SF. A follow-up study using the complete ALFALFA Hα data set is planned.

Environmental dependence of SF: It is known that galaxy morphologies show a trend with environment. Our data set samples a large range of galaxy environments, allowing for the
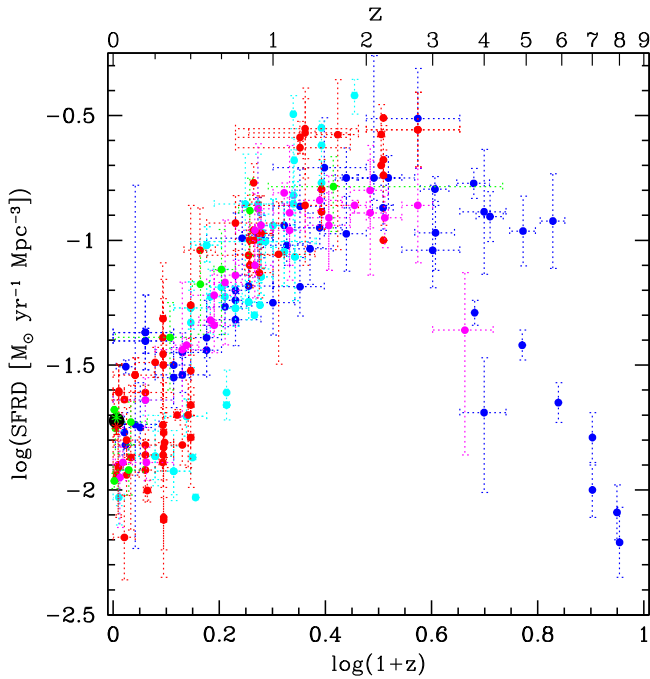
Figure 16. SFRD measurements across redshift. The colored points are from the literature and the black point is our measurement. (The random error bars for our measurement of the SFRD are smaller than the symbol size.) The different colors indicated different SFR measurement methods. red: Balmer lines (Hα/Hβ); blue: UV; cyan: Oxygen ([O II]/[O III]); magenta: IR; and green: Radio.

study of how SFRs and H I masses depend on local density. The size and completeness of our sample will allow for a more detailed study of the effect of environment on SFR than has been possible in the past. We have done a preliminary analysis exploring this topic with smaller samples and plan to explore this topic in future work.

Multi-wavelength SFR comparison: Comparing the differences in derived SFRs depending on the observed SF indicator is important. Understanding the differences between SF indicators facilitates more appropriate comparisons between studies done at different wavelengths. Our survey area overlaps with other surveys, such as *GALEX* (Gil de Paz et al. 2007) and *WISE*, which will be used to compare our Hα-derived SFRs with those derived using other wavelengths (e.g., UV and mid-infrared). We can also determine how using an internal absorption correction derived using different wavelengths affects derived SFRs. This study is currently in progress and the results are expected to be published in a forthcoming paper (A. Van Sistine et al. 2016, in preparation).

Modes of SF: This data set is perfect for studying the modes of SF in a comprehensive set of galaxies. We observe continuous SF in spiral arms in high-mass galaxies, but lower-mass galaxies that do not have spiral arms exhibit a more stochastic SF. Our data set could be used to explore what causes this transition in SF mode. In particular, we will be able to look at the transition in terms of many other properties of galaxies (e.g., H I and stellar mass, rotational velocities).

Chemical abundance studies: Our Hα images provide valuable maps of the H II regions in our sample galaxies, many of which will be interesting targets for follow-up spectroscopy. With spectroscopy, studies of metal abundances in galaxies as a function of H I mass and/or surface brightness, searches for ultra-low abundance systems, and the measurement of radial

abundance gradients in a comprehensive sample of galaxies all become possible. Examples of early nebular abundance studies of ALFALFA-related galaxies include Skillman et al. (2013) and Haurberg et al. (2013, 2015).

Hα Dots: Within our images there exist many point-like emission sources, "Hα dots." Follow-up spectroscopy of these sources (Kellar et al. 2012) reveals these sources to be a mix of compact, ultra-low luminosity systems at roughly the same velocity as the ALFALFA target, higher redshift star-forming galaxies or Seyfert 2s at $z \sim 0.3$ detected via strong [O III] $\lambda5007$ emission, or background QSOs. All three types of objects are intrinsically very interesting. An ongoing research program being carried out exclusively by undergraduate students has cataloged several hundred Hα Dots (J. Fedderson et al. 2016, in preparation), and follow-up spectroscopy now exists for roughly 250 objects.

7. SUMMARY

The ALFALFA Hα Survey uses an H I-selected sample of galaxies to study SF in the local universe. To minimize incompleteness corrections and limit any bias due to LSS density variations we designed our sample to be as close to volume-limited as possible and large enough to span a range of galaxy environments. Our sample is drawn from the ALFALFA α.40 sample (Haynes et al. 2011) and is divided into Fall and Spring samples. We have obtained narrowband Hα images for 1555 galaxies (565 in the Fall, 990 in the Spring). The H I masses of our sample of galaxies extend well below the knee of the HIMF out to our distance limit of $\sim$100 Mpc.

Our optical data were obtained using the WIYN 0.9 m and NOAO 2.1 m telescopes at KPNO. Each galaxy was observed using a narrowband Hα filter and a broadband R filter to measure the continuum. We use a locally developed pipeline to process our images and measure fluxes. In addition to measuring emission from the ALFALFA target galaxy, we also measured any emission from non-ALFALFA targets that are located in our images. We call these objects OTHERs and include them in our SFRD measurement in order to obtain the most comprehensive measurement of the local SFRD possible.

We apply several corrections to our fluxes to account for [N II] emission in the narrowband filter, Galactic extinction, and internal absorption. Both the [N II] and internal absorption corrections are statistical in nature and have been derived using the KISS database (e.g., Salzer et al. 2000, 2001).

We describe the corrections necessary to derive a local SFRD for our samples. To correct for the flux-limited nature of the ALFALFA survey, we use a $1/V_{max}$ correction. Our Fall sample did not require a correction to account for any galaxies with H I masses below the detection limit of ALFALFA. We also derive a LSS correction by comparing our volume to the complete α.40 volume out to 9500 km s^{-1}. This LSS correction is close to unity for the Fall sample.

Using our Fall sample, we have estimated the local SFRD. We adopt a SFRD of log(SFRD $[M_\odot$ yr^{-1} Mpc$^{-3}]$) = $1.747^{+0.029}_{-0.031}$ (random) ± 0.05 (systematic) that includes code 1 sources and their associated OTHERs in our volume. We then compared this value to others found in the literature and found that our measurement lies within the distribution of points but has significantly smaller error bars.

The ALFALFA Hα survey is a very useful data set that can be used for a wide range of purposes besides its primary

science goal. Many potential uses include the study of starburst galaxies within our sample, the study of the dependencies of SFR on galaxy environment, the comparison of SFR indicators at different wavelengths, the study of SF modes in galaxies, spectroscopic studies of abundances in H II regions, and the study of point-like emission sources in the images.

Our subsequent papers will present our data description and release (A. Van Sistine et al. 2016, in preparation; Paper 2), our local SFRD measurement based on our Spring sample (A. Van Sistine et al. 2016, in preparation; Paper 3), and an investigation of the SFR measurements at different wavelengths (A. Van Sistine et al. 2016, in preparation). The SFRD measured using the Spring sample will be an independent measurement of the local SFRD and will provide an excellent comparison to the measurement presented in this paper as well as a more thorough comparison with the literature.

REFERENCES

Adams, E. A. K., Faerman, Y., Janesh, W. F., et al. 2015, A&A, 573, L3
Adams, E. A. K., Giovanelli, R., & Haynes, M. P. 2013, ApJ, 768, 77
Ahn, C. P., Alexandroff, R., Allende Prieto, C., et al. 2012, ApJS, 203, 21
Barnes, D. G., Staveley-Smith, L., de Blok, W. J. G., et al. 2001, MNRAS, 322, 486
Bell, E. F. 2003, ApJ, 586, 794
Bennett, C. L., Larson, D., Weiland, J. L., et al. 2013, ApJS, 208, 20
Binggeli, B., Sandage, A., & Tammann, G. A. 1988, ARA&A, 26, 509
Bouwens, R. J., Illingworth, G. D., Oesch, P. A., et al. 2011, ApJ, 737, 90
Brinchmann, J., Charlot, S., White, S. D. M., et al. 2004, MNRAS, 351, 1151
Buat, V., Giovannoli, E., Takeuchi, T. T., et al. 2011, A&A, 529, A22
Cannon, J. M., Martinkus, C. P., Leisman, L., et al. 2015, AJ, 149, 72
Catinella, B., Schiminovich, D., Kauffmann, G., et al. 2010, MNRAS, 403, 683
Coe, D., Zitrin, A., Carrasco, M., et al. 2013, ApJ, 762, 32
Condon, J. J. 1992, ARA&A, 30, 575
Daddi, E., Dickinson, M., Morrison, G., et al. 2007, ApJ, 670, 156
Disney, M., & Phillipps, S. 1983, MNRAS, 205, 1253
Dressler, A. 1980, ApJ, 236, 351
Ellis, R. S., McLure, R. J., Dunlop, J. S., et al. 2013, ApJL, 763, L7
Fadda, D., Girardi, M., Giuricin, G., Mardirossian, F., & Mezzetti, M. 1996, ApJ, 473, 670
Gallego, J., García-Dabó, C. E., Zamorano, J., Aragón-Salamanca, A., & Rego, M. 2002, ApJL, 570, L1
Gallego, J., Zamorano, J., Aragon-Salamanca, A., & Rego, M. 1995, ApJL, 455, L1
Gallego, J., Zamorano, J., Rego, M., & Vitores, A. G. 1997, ApJ, 475, 502
Gavazzi, G., Fumagalli, M., Fossati, M., et al. 2013, A&A, 553, A89
Gavazzi, G., Fumagalli, M., Galardo, V., et al. 2012, A&A, 545, A16
Geller, M. J., Kurtz, M. J., Wegner, G., et al. 1997, AJ, 114, 2205
Gil de Paz, A., Boissier, S., Madore, B. F., et al. 2007, ApJS, 173, 185
Giovanelli, R., Haynes, M. P., Adams, E. A. K., et al. 2013, AJ, 146, 15
Giovanelli, R., Haynes, M. P., Kent, B. R., et al. 2005, AJ, 130, 2598
Gronwall, C. 1999, in AIP Conf. Proc. 470, After the Dark Ages: When Galaxies Were Young, ed. S. Holt & E. Smith (New York: AIP), 335
Gronwall, C., Jangren, A., Salzer, J. J., Werk, J. K., & Ciardullo, R. 2004a, AJ, 128, 644
Gronwall, C., Salzer, J. J., Sarajedini, V. L., et al. 2004b, AJ, 127, 1943
Gunawardhana, M. L. P., Hopkins, A. M., Bland-Hawthorn, J., et al. 2013, MNRAS, 433, 2764
Hanish, D. J., Meurer, G. R., Ferguson, H. C., et al. 2006, ApJ, 649, 150
Haurberg, N. C., Rosenberg, J., & Salzer, J. J. 2013, ApJ, 765, 66
Haurberg, N. C., Salzer, J. J., Cannon, J. M., & Marshall, M. V. 2015, ApJ, 800, 121
Haynes, M. P., Giovanelli, R., Martin, A. M., et al. 2011, AJ, 142, 170
Hogg, D. W., Cohen, J. G., Blandford, R., & Pahre, M. A. 1998, ApJ, 504, 622
Hopkins, A. M. 2004, ApJ, 615, 209
Hopkins, A. M., & Beacom, J. F. 2006, ApJ, 651, 142
Huang, S., Haynes, M. P., Giovanelli, R., & Brinchmann, J. 2012, ApJ, 756, 113
Impey, C., & Bothun, G. 1997, ARA&A, 35, 267
James, P. A., Knapen, J. H., Shane, N. S., Baldry, I. K., & de Jong, R. S. 2008, A&A, 482, 507
James, P. A., Shane, N. S., Beckman, J. E., et al. 2004, A&A, 414, 23
Jangren, A., Salzer, J. J., Sarajedini, V. L., et al. 2005a, AJ, 130, 2571
Jangren, A., Wegner, G., Salzer, J. J., Werk, J. K., & Gronwall, C. 2005b, AJ, 130, 496
Janowiecki, S., Leisman, L., Józsa, G., et al. 2015, ApJ, 801, 96
Jarrett, T. H., Masci, F., Tsai, C. W., et al. 2013, AJ, 145, 6
Jaskot, A. E., Oey, M. S., Salzer, J. J., et al. 2015, ApJ, 808, 66
Kellar, J. A., Salzer, J. J., Wegner, G., Gronwall, C., & Williams, A. 2012, AJ, 143, 145
Kennicutt, R. C., & Evans, N. J. 2012, ARA&A, 50, 531
Kennicutt, R. C., Jr. 1998, ARA&A, 36, 189
Kennicutt, R. C., Jr., Lee, J. C., Funes, S. J., et al. 2008, ApJS, 178, 247
Kistler, M. D., Yüksel, H., Beacom, J. F., Hopkins, A. M., & Wyithe, J. S. B. 2009, ApJL, 705, L104
Lang, R. H., Boyce, P. J., Kilborn, V. A., et al. 2003, MNRAS, 342, 738
Lilly, S. J., Le Fevre, O., Hammer, F., & Crampton, D. 1996, ApJL, 460, L1
Madau, P., & Dickinson, M. 2014, ARA&A, 52, 415
Madau, P., Ferguson, H. C., Dickinson, M. E., et al. 1996, MNRAS, 283, 1388
Martin, A. M., Papastergis, E., Giovanelli, R., et al. 2010, ApJ, 723, 1359
Massey, P., Strobel, K., Barnes, J. V., & Anderson, E. 1988, ApJ, 328, 315
Masters, K. L. 2005, PhD Thesis, Cornell University
McQuinn, K. B. W., Skillman, E. D., Cannon, J. M., et al. 2010, ApJ, 721, 297
Meurer, G. R., Hanish, D. J., Ferguson, H. C., et al. 2006, ApJS, 165, 307
Meurer, G. R., Heckman, T. M., & Calzetti, D. 1999, ApJ, 521, 64
Meyer, M. J., Zwaan, M. A., Webster, R. L., et al. 2004, MNRAS, 350, 1195
Moustakas, J., Kennicutt, R. C., Jr., & Tremonti, C. A. 2006, ApJ, 642, 775
Nakamura, O., Fukugita, M., Brinkmann, J., & Schneider, D. P. 2004, AJ, 127, 2511
Oesch, P. A., Bouwens, R. J., Illingworth, G. D., et al. 2014, ApJ, 786, 108
Osterbrock, D. E., & Ferland, G. J. 2006, Astrophysics of Gaseous Nebulae and Active Galactic Nuclei (2nd ed.; Sausalito, CA: Univ. Science Books)
Pérez-González, P. G., Cava, A., Barro, G., et al. 2013, ApJ, 762, 46
Planck Collaboration, Ade, P. A. R., Aghanim, N., et al. 2014, A&A, 571, A16
Ranalli, P., Comastri, A., & Setti, G. 2003, A&A, 399, 39
Saintonge, A. 2007, AJ, 133, 2087
Salim, S., Rich, R. M., Charlot, S., et al. 2007, ApJS, 173, 267
Salpeter, E. E. 1955, ApJ, 121, 161
Salzer, J. J., Gronwall, C., Lipovetsky, V. A., et al. 2000, AJ, 120, 80
Salzer, J. J., Gronwall, C., Lipovetsky, V. A., et al. 2001, AJ, 121, 66
Salzer, J. J., Jangren, A., Gronwall, C., et al. 2005, AJ, 130, 2584
Schiminovich, D., Catinella, B., Kauffmann, G., et al. 2010, MNRAS, 408, 919
Schlafly, E. F., & Finkbeiner, D. P. 2011, ApJ, 737, 103
Schlegel, D. J., Finkbeiner, D. P., & Davis, M. 1998, ApJ, 500, 525
Skillman, E. D., Salzer, J. J., Berg, D. A., et al. 2013, AJ, 146, 3
Spaenhauer, A. M. 1978, A&A, 65, 313
Spector, O., Finkelman, I., & Brosch, N. 2012, MNRAS, 419, 2156
Sullivan, M., Treyer, M. A., Ellis, R. S., et al. 2000, MNRAS, 312, 442
Tresse, L., & Maddox, S. J. 1998, ApJ, 495, 691
van Dokkum, P. G. 2001, PASP, 113, 1420
Véron-Cetty, M.-P., & Véron, P. 2010, A&A, 518, A10
Wegner, G., Salzer, J. J., Jangren, A., Gronwall, C., & Melbourne, J. 2003, AJ, 125, 2373
Wen, X.-Q., Wu, H., Zhu, Y.-N., et al. 2014, MNRAS, 438, 97

Westra, E., Geller, M. J., Kurtz, M. J., Fabricant, D. G., & Dell'Antonio, I. 2010, ApJ, 708, 534

Wilson, G., Cowie, L. L., Barger, A. J., & Burke, D. J. 2002, AJ, 124, 1258

Wright, E. L., Eisenhardt, P. R. M., Mainzer, A. K., et al. 2010, AJ, 140, 1868

York, D. G., Adelman, J., Anderson, J. E., Jr., et al. 2000, AJ, 120, 1579

Yüksel, H., Kistler, M. D., Beacom, J. F., & Hopkins, A. M. 2008, ApJL, 683, L5

Yun, M. S., Reddy, N. A., & Condon, J. J. 2001, ApJ, 554, 803